行政院國家科學委員會專題研究計畫 成果報告

利用重力及GPS觀測台灣造山運動
研究成果報告(精簡版)

計 畫 類 別 ：個別型
計 畫 編 號 ：NSC 97-2116-M-009-001-
執 行 期 間 ：97年08月01日至98年07月31日
執 行 單 位 ：國立交通大學土木工程學系（所）

計 畫 主 持 人：黃金維
共 同 主 持 人：趙丰
計畫參與人員：博士班研究生-兼任助理人員：高瑞其
博士班研究生-兼任助理人員：謝文祺
博士後研究：鄭景中
博士後研究：潮見幸江

報 告 附 件 ：出席國際會議研究心得報告及發表論文

處 理 方 式 ：本計畫可公開查詢

中 華 民 國 98年10月29日

行政院國家科學委員會補助專題研究計畫 ■ 成 果 報 告
□期中進度報告

利用重力及GPS觀測台灣造山運動

計畫類別：■ 個別型計畫　□ 整合型計畫
計畫編號：NSC 97 － 2116 － M － 009 － 001 －
執行期間： 97 年 8 月 1 日至 98 年 7 月 31 日

計畫主持人：黃金維
共同主持人：趙丰
計畫參與人員： 鄭景中、潮見幸江、高瑞其、謝文祺

成果報告類型(依經費核定清單規定繳交)：■精簡報告　□完整報告

本成果報告包括以下應繳交之附件：
□赴國外出差或研習心得報告一份
□赴大陸地區出差或研習心得報告一份
■出席國際學術會議心得報告及發表之論文各一份
□國際合作研究計畫國外研究報告書一份

處理方式：除產學合作研究計畫、提升產業技術及人才培育研究計畫、列管計畫及下列情形者外，得立即公開查詢
□涉及專利或其他智慧財產權，□一年□二年後可公開查詢

執行單位：國立交通大學

中　華　民　國　98　年　10　月　28　日

目　錄

圖 目 錄

表 目 錄

1. 前言

台灣位於歐亞板塊及菲律賓海板塊交界，屬於環太平洋活躍的造山帶之一，由GPS 觀測知（Yu et al., 2003）菲律賓海板塊以每年7公分速度向西北方向前進，在台灣東南部造成約每年1-2公分的板塊抬昇(Hwang and Hwang, 2002)，此抬昇量在觀測條件良好情況，可由GPS 或水準測得。但GPS 或水準僅可提供板塊幾何的知識，深層或整體板塊的變遷則需要其他如地震監測或重力資料之配合解釋。台灣西部斷層的成因是由於板塊推擠所造成(Teng, 1990)。

內政部於2006年為配合國家重力基準站的建立及國家重力網之建置(黃金維, 2009)，在南橫、綠島及台南建立了10個絕對重力點(表1, 圖1)，由法國Frederic Masson 教授為首的一群地球物理學家對台灣的造山運動極為有興趣，雙方合作採用重力為主，GPS 為輔的方法，進行台灣造山運動之研究; Masson 教授在伊朗、葉門及非洲已有進行過類似研究。台灣的交大－中央大－工研院團隊在絕對重力儀FG5、相對重力儀EG及GPS之觀測及資料處理上已累積數年之經驗，由過去的經驗得知，在南橫地區的重力觀測精度可達1μgal ($10^{-8}ms^{-2}$)。

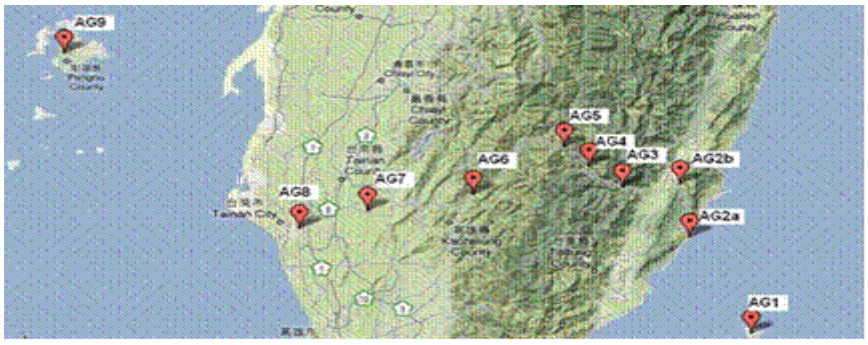

圖 1 南橫 AGTO 點位分佈

表 1：點位坐標及所在縣市

點號	點名	97 坐標(Lat,Lon,Elev)	所在縣市
AG1	綠島	緯度:22.658 經度:121.476 高度：4m	台東縣
AG2a	東河國小	緯度:22.970 經度:121.300 高度：50m	台東縣
AG2b	富里	緯度:23.142 經度:121.280 高度：378m	花蓮縣
AG3	新武橋	緯度:23.133 經度:121.119 高度：409m	台東縣
AG4	摩天	緯度:23.201 經度:121.026 高度：1622m	台東縣
AG5	埡口	緯度:23.264 經度:120.961 高度：2762m	台東縣
AG6	寶來國中	緯度:23.109 經度:120.706 高度：410m	高雄縣
AG7	左鎮國中	緯度:23.057 經度:120.412 高度：51m	台南縣
AG8	成功大學	緯度:22.999 經度:120.220 高度：62m	台南市
AG9	澎湖	緯度:23.565 經度:119.563 高度：18m	澎湖縣

2. 研究目的

為探索台灣地貌之形成，可以從地貌隆起、侵蝕、搬運及堆積作用來推測，但對於造山運動的機制及成因卻較少有數據可以參考，近年來由於GPS的成熟發展，已經有許多研究利用GPS、水準測量及InSAR 等技術來監測幾何上的形變（蔡義本，民93）。集集地震的成因，不只是地殼錯動所造成之地震還可能是台灣的造山運動所造成之原果(Kao, 2000)。

利用重力及GPS數據資料在板塊動力學上解釋板塊模式理論的模擬與探討是由法方提供，台灣方面主要是針對重力資料改正分析發展以重力反衍，驗證地球物理現象的技術。

3. 文獻探討

3.1. 台灣地區板塊構造背景

台灣位處於菲律賓海板塊與歐亞大陸板塊交界處，同時是菲律賓海板塊上呂宋火山島弧(Luzon arc)向歐亞大陸板塊邊緣延伸的聚合點。在東北側，菲律賓海板塊隱沒進歐亞大陸板塊之下；這可從琉球海溝得到驗證。另一方面，在南邊兩個板塊的交界，歐亞大陸板塊則隱沒入菲律賓海板塊之下，且形成了馬尼拉海溝(Angelier,1990)。在陸地上，台灣花東縱谷正是這兩個板塊交接的分界線。呂宋火山島弧和歐亞大陸板塊邊緣的碰撞大約自6千5百萬年前開始發生。由於兩個板塊的斜向交會，這個碰撞以每年31mm的速度向南推進(Simoes & Avouac, 2006)。台灣的造山運動已累積了約4000公尺的高度，且不斷的繼續增長(圖2)。

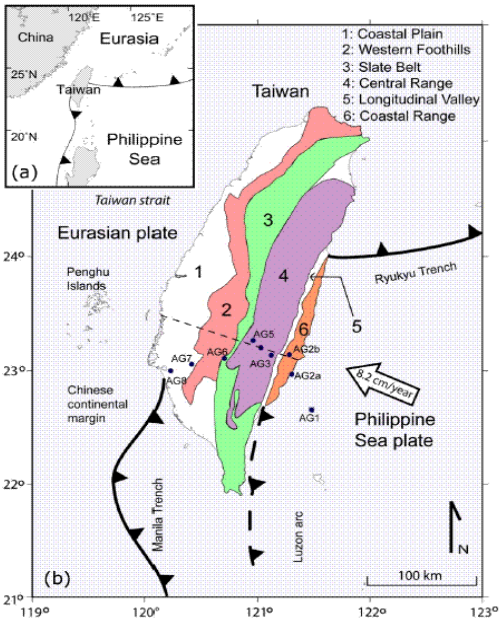

圖 2 板塊碰撞的邊界與推移方向。五個地質區以顏色區分。9 個編號 AG 之點位為絕對重力觀測點。橫斷台灣的虛線為模型剖面位置

3.2. 薄皮模型及厚皮模型的理論

根據Chapple(1978)及其他學者推想的薄皮模型的理論(thin skin tectonic)，台灣地區板塊移動層的分界面應當在新第三紀(Neogene)層的深度。西側移動境界面的位置約在深度10公里處，一既沈積層的底部。向東逐漸向深處隱沒在中央山脈下方。此模型中所有斷層皆不超過移動境界面。在這種模型的設定下，板塊交界處推擠所產生的隆起相當類似推土機推刀前的堆積。根據這樣的模型，可以推估地表形變的狀況(Davis et al., 1983)，這些推估的結果與野外調查的結果相當吻合。Dahlen等人(1984)更進一步推論這個移動分界面應當位處第三紀中新世(Miocene)層與第三紀上新世(Pliocene)層間的深度，近年來有更多的學者就薄皮模型的假設推論更詳盡的剖面結構(Malavieille＆Trullenque,2007)。

另外有些學者根據台灣的震源分佈資料，鑽探資料，與震測資料（Hung et al., 1999），提出了截然不同的厚皮機制模型，這個模型推定板塊移動的境界面在更深的地殼底部。根據這樣的模型，板塊擠壓的變形會伴隨著一些正斷層轉變成逆衝斷層的作用。相關的研究(Wu et al,1997)指出，台灣地區的造山運動包含了整個地殼，以及上部地函(upper mantle)-尤其在中央山脈的地區；相較於薄皮模型，移動境界面位於比較深的地方，大約是靠地殼與上部地函的交界處。為了合理解釋厚皮機制所造成的變形，板塊移動的境界面必須是地殼中結構相對較弱的部份，極可能為硬脆與延展性層次間的不連續面。這個研究並不計畫在理論爭議中全然的支持或否決其中一個理論，而是希望藉由兩種理論機制所衍生的重力場，比對實際觀測的重力數據與 GPS 數據，藉由觀測數據改良理論細節，作為板塊構造研究一個新的探討方向。

3.3. 斷層模型的計算

在完成模型設定以後，Okada(1985,1992)的數學模式可用來計算由斷層滑移所造成地表的水平與垂直位移。斷層的幾何構形與移動方向可在計算前加以設定。依照所得到台灣地區地球物理，地質資料，這些參數被小心的調整使計算模式能夠趨近實際的狀況。在初步的實驗裡，參數的設定原則包括：

1. 斷層的位置依照台灣地質圖的資料設定，所有的斷層皆容許逆向運動。
2. 東側板塊滑移的速率依照菲律賓海板塊移動速度，每年82㎜的參考值設定。
3. 板塊移動的速率由東向西遞減。
4. 斷層的設定從地表開始一直延伸到板塊位移的境界面。程式的設定可以容許一個斷層面有兩段不同的幾何結構。在不同的深度可以有不同的斷層滑移速度。
5. 大部分斷層在地表皆無滑移，但東縱谷斷層在地表仍設定每年30㎜滑移量。
6. 在花東縱谷之外，西部丘陵的斷層設定有較多的滑移量。

根據這些設定，針對兩種板塊運動機制，我們可預估地表的水平與垂直變化。這個預估量可以拿來與GPS連續追蹤站的資料相互比較。然而，必須要強調的，在本研究展示的變形模型僅是初步用來說明的1維剖面簡化版本，所以只考慮菲律賓海板塊隱沒到歐亞大陸板塊的情形。在後續的研究中，我們會將2維的模型推展到3維的狀況，並納入更多複雜的考量。

3.4. 板塊運動的重力效應

由於 GPS 在高程定位上需要長時間大量觀測資料以達成所需精度，重力觀測正可提供幾何位移或物理異變量的資訊。我們使用程式 GRANOM 來計算理論上板塊運動造成變形後所相應的重力效應。這個程式是依照 Won 和 Bevis(1987)的演算法則編寫而成，可計算 2 維剖面裡彈性變形前的重力值與變形後的重力值。兩個重力值的差值極為板塊運動所相應的重力效應。GRANOM 的計算需要剖面上的密度分佈資料。根據台灣五個地質區域，根據斷層的分界，我們可採表 2 所列的密度設定。

表 2：密度設定模式

區域	密度 kg m^{-3}
西部海岸平原	2500
西部丘陵，Slate belt，中央山脈	2700
海洋地殼（包含海岸山脈）	2800

另一方面，模型裡沿垂直方向上的密度分佈變化(圖 3)，原則上以由淺至深逐漸增加做為設定原則。針對兩種板塊模型，其彈性變形效應所衍生的重力剖面顯示在圖 3b，主要包含了自由空間位移效應(fee air effect)與板片效應(plate effect)，這兩個效應每年可達 3 個 μGal 的增量。經過移除自由空間效應後的重力剖面展現在圖 3a，呈現了變形部分質量所產生的引力。在對照以 GPS 或其他方式得到的地表幾何位移量之下，可以驗證變形部分的密度值。

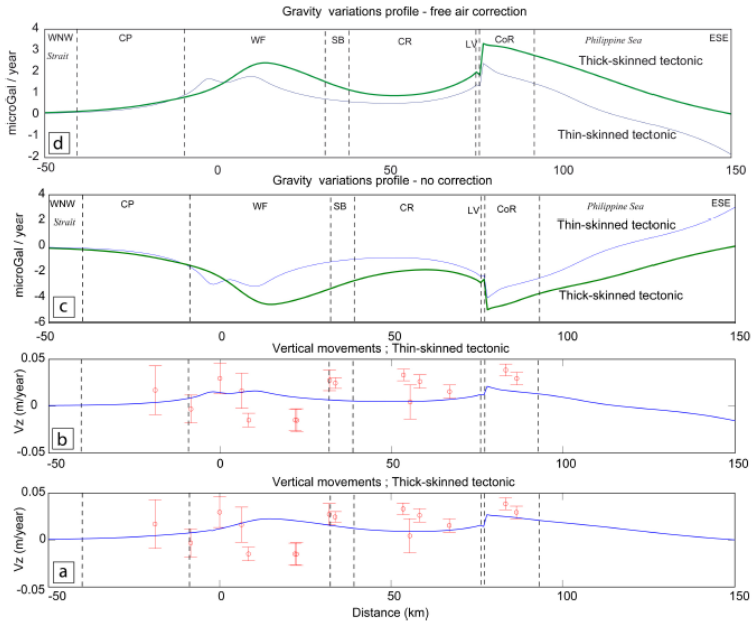

圖 3 (a)厚皮模型之垂直位移(b)薄皮模型之垂直位移(c)垂直位移所產生之重力效應(d)去除自由空間位移效應後之重力殘值

如果更進一步假定了變形部分的平均密度，並把相應的重力效應移除後，剩下的殘值呈現了深部的質量轉移，或稱密度分佈變化。這個殘量相對應於自由空

間位移效應與板片效應而言，相當微弱。厚皮模型所產生的質量轉移效應較大，可達每年 0.3 μGal 的程度；而薄皮模型的質量轉移效應則趨近於零。以厚皮模型而言，東部地區的質量轉移訊號來自於密度較大的海洋板塊，包括海岸山脈，在中央山脈下向西側擴張的結果。而西部平原與丘陵下的質量轉換可能源自於在板塊位移境界面的深度下部地殼與上部地函質量交換所產生的效果(圖 4)。

在後續的研究裡，以 GPS 觀測站與相對，絕對重力點組成的監測網將提供幾何位移，質量重分佈的資訊，作為約制理論模型的條件。例如非彈性的應變，並且藉由觀測數據的空間關連性將 1 維剖面拓展成面狀涵蓋的模型。

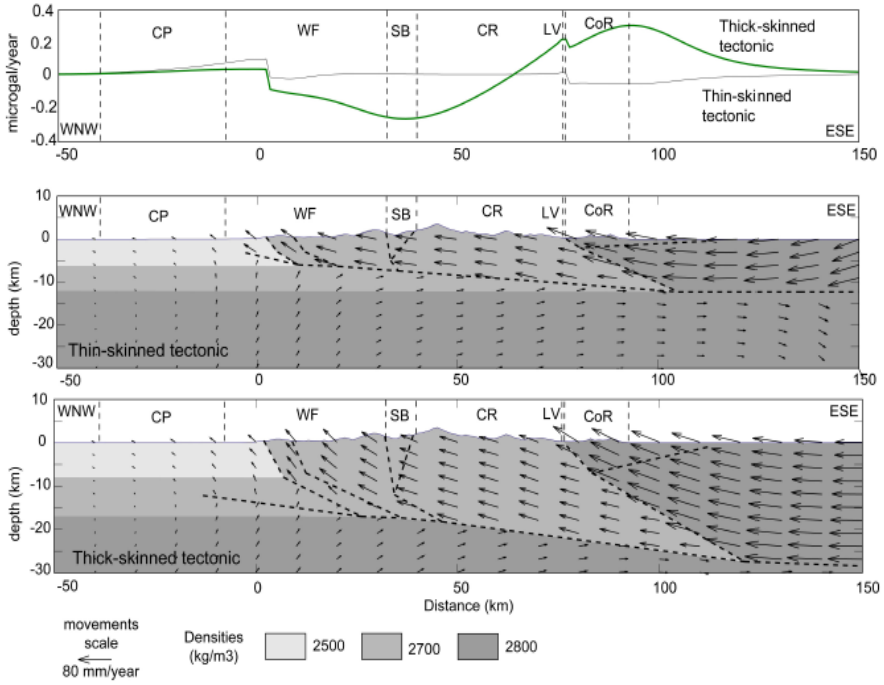

圖 4 移除自由空間效應與板片效應後，殘餘的質量轉移效應。厚皮模型(綠線)在海岸山脈預期將會有最大達 0.3 μGal/year 的訊號（上圖）。薄皮模型(中圖)與厚皮模型(下圖)的質量轉移向量圖

因為台灣島來自海洋，板塊互相推擠運動造成了地殼的隆起而成為陸地，由於台灣現今利用GPS 等測量所得的構造運動型態與造山速率相對於幾萬年、幾百萬年之造山運動速率相異甚大，加上氣候影響山脈侵蝕造成土石流，山區的地貌也會持續變化，所以單純從幾何上來對於造山運動之解釋，沒有考慮到地底內部質量變化，在說造山運動過程中有些現象解釋會有盲點，像是在監測青藏高原的隆升利用了絕對重力儀FG5，從1993 年至1999 年重力值減小了$12\times10^{-8}ms^{-2}$，証實拉薩的上升速率為10mm/year(張為民,2000)。

事實上在台灣島的四周海域內，東北方有沖繩海槽，南方有呂宋島弧等海底構造，全都在影響著台灣島的形成，而台灣島構造依地質來區分，也可以清楚的看出台灣的構造和縱切台灣的幾條斷層線是有很大的關係的。

中國在1982~1996 年期間也曾用LaCoste-G型相對重力儀在成都-拉薩做過多次重覆的相對重力，但其精度不如絕對重力儀FG5，高精度之絕對重力測量有二

個優勢：一是它反應地面上某點的地殼垂直形變，且提供該點下方物質運動之訊息；其次是它所量到的是地表相對於大地水準面的垂直變化。

本計畫是利用重力及GPS 來分析造山運動之成因，跨越了東部海岸山脈、花東縱谷、中央山脈、西部麓山帶及西部海岸平原，可以說將整個台灣主要的結構都做了深入的量測及分析，除了空間幾何上的原因之外，還考慮到地底下質量運動所帶來重力變化，而影響重力變化之成因包含了固體潮、海潮負載、大氣壓力、地下水位、極運動及其他環境因素之影響，本團隊對於環境影響之改正經驗，有助於將FG5所測得之絕對重力值，用來建立台灣更完善之環境改正模式。

4. 研究方法

4.1. 南橫重力加密計算

相對重力觀測補強該區域之重力密度，選取沿公路之一等水準點利用相對重力儀做觀測，以階梯式做往返之觀測。其步驟如表3.

表 3：相對重力儀操作流程

項次	工作項目	工作確認
1	規劃	整合全部測區內之所有重力觀測資料，以絕對重力點位作為約制，對所有重力觀測點作加權約制平差計算，求得各觀測點之重力值。
2	開始測量	重力網平差過程中，通常會選定一個或一個以上的固定點(絕對重力點)作為平差時的約制點，以確保所有的未知點位皆位於同一基準上。
3	計算	加權約制平差之計算模式，係平差前能給該約制點先驗變方值（priori variances），亦即一個適當的權值，用來控制平差過程中的誤差量。
4	約制	在加權約制平差的過程中，約制用控制點之未知參數所組成的設計矩陣2 A 為一特殊類型矩陣，其行數（columns）和列數（rows）皆等於未知參數個數（令為n），而x P 為約制用控制點之權值所組成的對角線矩陣，其維數為$n\times n$ 。
5	$n\times n$ 矩陣	所以 $A_2^T P_x A_2$ 與 $A_1^T P_1 A_1$ 也是$n\times n$ 維矩陣。以符號 $\overline{P}_x$ 代替 $A_2^T P_x A_2$，那 $\overline{P}_x$ 為一個除了相對於約制用控制點未知參數之對角線上元素值為+1外，其餘元素都為零的$n\times n$矩陣。

例如，以 X_2 、X_3 為控制點，也就是分別以第二和第三個未知參數為控制點，故

$$\overline{P}_x = \begin{bmatrix} 0 & 0 & 0 & . & . \\ 0 & 1 & 0 & . & . \\ 0 & 0 & 1 & . & . \\ . & . & . & . & . \\ . & . & . & . & . \end{bmatrix}$$

因 $A_2^T P_x A_2 = \overline{P}_X$ ，所以

$$A_1^T P_1 A_1 + A_2^T P_1 A_2 = A_1^T P_1 A_1 + \overline{P}_X \qquad (4\text{-}1)$$

由上式得知，控制點的權值可直接加入法方程矩陣（normal equation matrix）中相對於約制用控制點之未知參數的對角線元素。當控制點之權值相當大或無限大時，平差後 $\hat{X}_2$ 會與平差前所給予的控制點值相當接近，即 V_X 趨近於零。本研究中之絕對重力點作為平差計算之約制點，計算出其他由相對重力法所引測之 20 個點位重力值。相關理論見 Koch（1987）。

依不同的點位分佈(圖 5)，可以分成階段、階梯式、改良式階梯式、星狀式及線狀式等方式來成做重力量測。

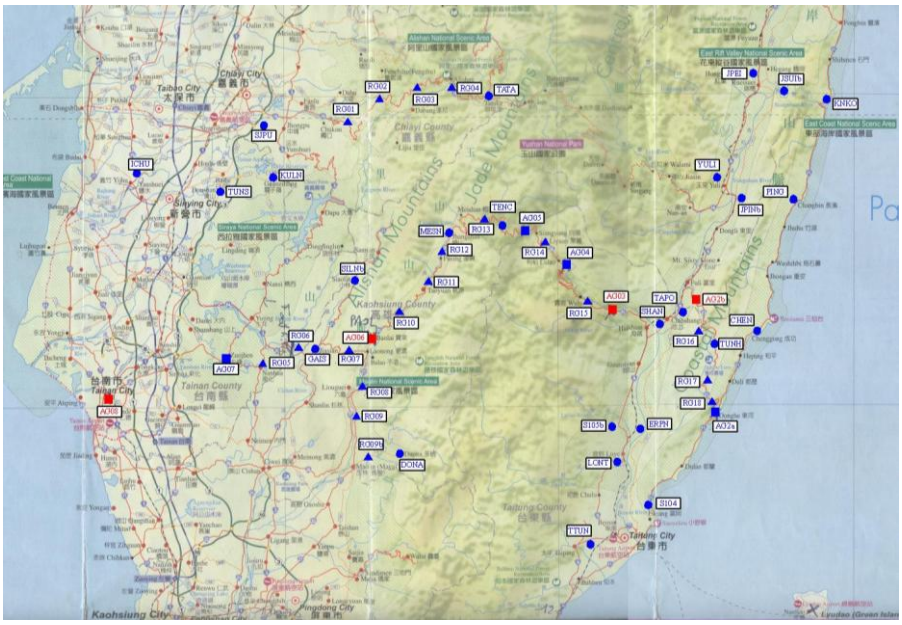

圖 5 南橫公路沿線相對重力測量路線圖

4.2. 薄皮模型的模擬計算

板塊的移動境界面在西部海岸設定為 5 公里深，線性遞增到海岸山脈下的 10 公里深(圖 6a)。根據這樣的設定，計算出的地表水平位移與 GPS 水平速度有相當不錯的吻合度(圖 6b)。垂直位移上則在西部丘陵與西部海岸平原顯示了較大的歧異(圖 6c)。由於薄皮模型中斷層的深度較淺，所以會產生較大的水平位移與較小的垂直位移。根據各種嘗試錯誤的方式探討模型的設定後發現，若將板塊移動境界面的深度設得淺一點，地表的水平位移量可以與 GPS 的觀測量有更佳的吻

合。

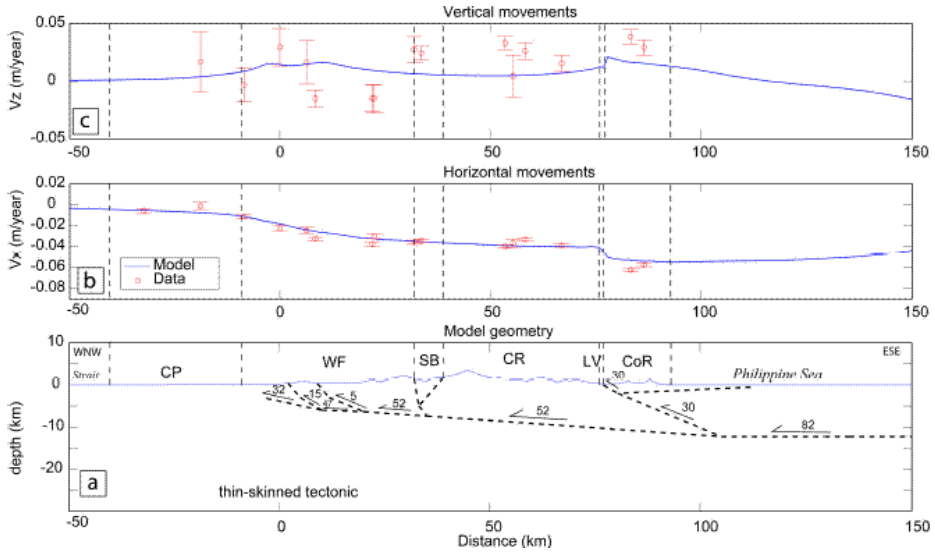

圖 6 由下而上，(a)薄皮模型剖面之斷層，板塊移動境界面之狀況。(b)模型推估之沿剖面方向水平位移，以向東邊為正。紅色符號表實際觀測量與其觀測誤差上下界(c)模型推估之垂直位移。可見紅色標示之觀測量有較大之散佈

4.3. 厚皮模型的模擬計算

根據各種嘗試計算，我們把厚皮模型在西部的板塊位移境界面深度設在 15 公里處(圖 7a)，向東以 3 度的角度遞增。

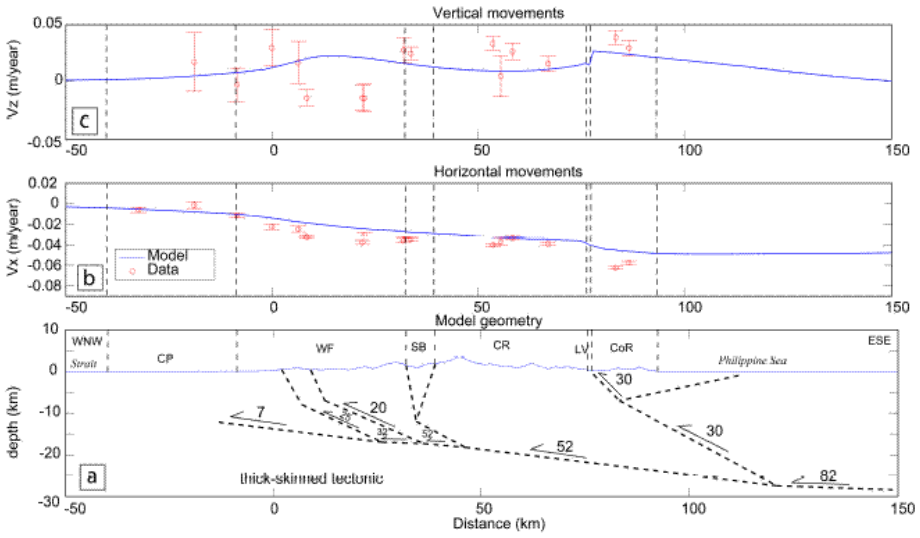

圖 7 厚皮模型剖面的理論與實際觀測比較

厚皮模型的斷層有較深的深度，所以深部斷層的滑移減輕了地表的變形量。這個模型的計算結果在西部丘陵與海岸山脈兩區的水平位移量較 GPS 的觀測明顯低估(圖 7b)。相較之下，垂直位移則有較明顯的訊號(圖 7c)。與圖 6 之薄皮模型相較，厚皮模型在水平方向的位移與實際觀測有較大的不一致。

5. 結果與討論

選定本計畫內之博士生擔任外業觀測之負責人,每次外業要先撰寫行程計畫書,為了消除氣候環境影響重力變化外,還要在出發前注意天氣預報,是否會有鋒面或是下雨的機會。最後將歷年來之成果整理如表4。

表 4：AGTO 絕對重力值一覽表

點號	2006 年		2007 年		2008 年	
	絕對重力值 (μGal)	不確定度 (μGal)	絕對重力值 (μGal)	不確定度 (μGal)	絕對重力值 (μGal)	不確定度 (μGal)
AG1	*836.6	4.4	*840.7	6.5	*837.1	4.3
AG2a	*578.4	4.3	*582.0	4.4	*577.5	4.3
AG2b	*495.3	4.4	*498.7	4.3	*493.4	4.3
AG3	*025.2	4.4	*015.0	4.3	*010.6	4.3
AG4	*874.9	4.3	*872.8	4.3	*879.7	4.3
AG5	*960.3	4.3	*959.0	4.4	*962.3	4.3
AG6	*869.1	4.3	*866.5	4.4	*871.1	4.3
AG7	*377.1	4.3	*378.1	4.8	*375.1	4.3
AG8	*243.3	4.5	*196.7	4.9	*233.3	4.4
AG9	無	無	*717.1	4.6	*716.0	4.4
註：絕對重力值換算至基樁面 0 公分高度，假設重力梯度-3.0 μGal / cm *代表省略之前的數值，不是相同的數值						

目前已完成 3 年次 AGTO 觀測作業，2006 年與 2008 年使用法方絕對重力儀 FG5-228；2007 年使用內政部絕對重力儀 FG5-224。圖 8 顯示各點位重力值之前 3 年來趨勢，目前點位變化不明顯，但 AG3 卻有明顯的重力變小趨勢，其位於中央山脈，應與點位 AG4、點位 AG5 有類似趨勢，但結果不然，值得持續觀察。另 AG8 位於台南市內，背景雜訊較大，重力值變動大，值得持續觀測，探究原因。在相對重力方面，觀測網總共包含 9 個相對重力線(圖 5)，由南橫公路主線向南北延伸。2008 年 11 月已使用相對重力儀 CG5 進行第一次觀測，觀測經平差後各監測點重力值列於表 5。第二次觀測預計將於 2009 年 11 月進行。伺第二次觀測完成後，將有間隔一年之重力差值，可進行初步的板塊模型分析驗證。

由於本計畫是和法國展開三年以上之長期合作，2010年由法方運FG5－228來台量測絕對重力、相對重力及GPS，2009及2011年由台灣團隊負責攜帶FG5-224至絕對重力點上量測，目前計畫在每年的十一月做絕對重力測量，而EG 及GPS則在這時間點附近做完，最終的成果是要做出台灣的地體動力模式。

本計畫是長期監測南橫之重力及 GPS 變化，而南橫通過海岸山脈斷層南段、玉里斷層、中央山脈斷層、左鎮斷層、觸口斷層及新化斷層等，由於活斷層對於地表會有二種破壞機制，分別是地盤的錯動和異常激烈的地震動（侯進雄,

2004）。

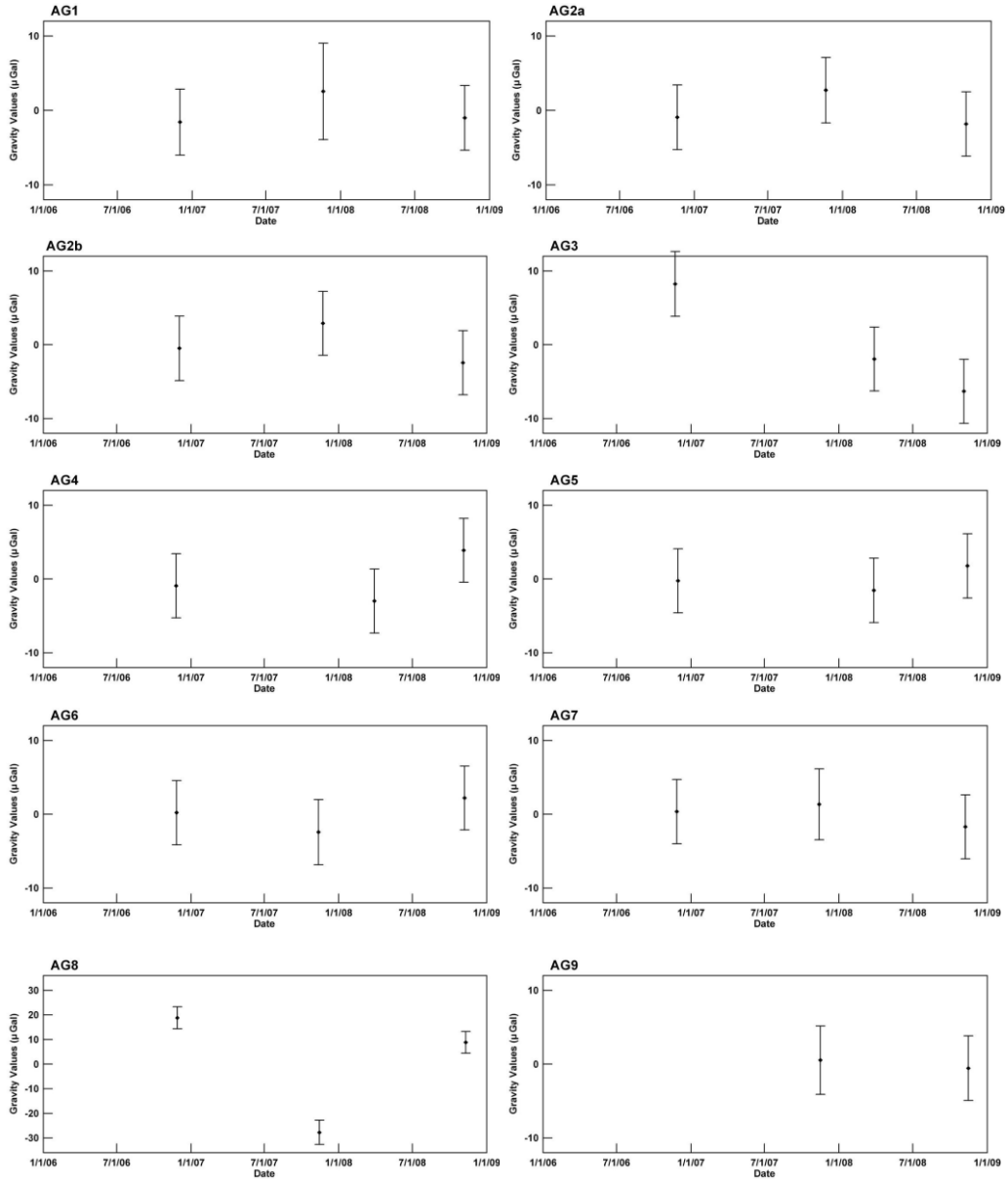

圖 8 AG 各點位重力值變化

本計畫之成果將有助於提供地質學在地震防災的研究上有更多的參考資料，對於基礎地球科學的研究也提供重要的數據，經過長時間的國際合作預期未來的成果能達到：

一、利用實測資料來分析台灣造山運動之成果。並將成果分享各相關領域，期望推廣重力量測，利用重力量測之方式能以較經濟的方式來監測台灣斷層及地質的變化。

二、加入全球地體動力計畫，將台灣現有之超導重力、絕對重力及相對重力之成果，能自行分析及應用，提昇台灣自有研究之能力。

三、由於災害預防之觀念已日趨重要，各山區在經過數次颱風及地震之侵襲下，造成許多土石流、斷橋、地基流失等問題，而重力量測可以在地質變化之初期即偵測得到，達到預警的功效。

表 5　2008 年 11 月相對重力網平差數據一覽表，此平差計算以南橫主線上 9 個絕對重力點重力觀測為基準約制。該重力網包含 9 個相對重力線 52 個監測點。

longitude(◦)	latitude(◦)	gravity(mili gal)	site ID
120.27920	23.35806	978832.502	ICHUb
120.40469	23.31761	978816.260	TUNS
120.50790	23.33044	978749.334	KULNb
120.48159	23.42754	978818.635	SJPUb
120.61140	23.43346	978761.845	RG01
120.68912	23.46288	978569.017	RG02
120.76638	23.48967	978488.330	RG03
120.82280	23.48678	978353.639	RG04
120.88980	23.48737	978280.153	TATAb
120.63335	23.06984	978675.987	RG07
120.59144	23.08053	978747.991	GAISb
120.64270	23.16277	978729.013	SILNb
120.55424	23.06750	978741.869	RG06
120.48568	23.05493	978773.514	RG05
120.41200	23.05700	978794.394	AG07
120.65671	23.00625	978743.244	RG08
120.65133	22.96367	978745.562	RG09
120.65680	22.88599	978748.469	RG09b
120.70353	22.91562	978690.447	DONA
120.70289	23.10860	978713.821	AG06
120.73860	23.13808	978685.266	RG10
120.77597	23.16941	978669.807	RG11
120.80254	23.22153	978648.455	RG12
120.82630	23.26380	978611.794	MESN
120.87675	23.28170	978449.120	RG13
121.06504	23.15316	978669.312	RG15
121.02600	23.20100	978491.018	AG04
120.98627	23.24797	978340.814	RG14
120.96058	23.26388	978248.983	AG05
120.91727	23.27698	978344.389	TENCb
121.29535	22.98927	978881.430	RG18
121.30060	23.04509	978863.194	RG17
121.30020	23.07556	978830.176	TUNH
121.27246	23.10294	978770.386	RG16
121.23711	23.12160	978817.210	TAPOb
121.19951	23.10886	978812.165	SHAN
121.30465	22.97043	978893.609	AG2a

表 5 (續)

121.37475	23.09881	978916.917	CHENb
121.45436	23.31944	978895.619	PING
121.50578	23.47243	978902.603	KNKO
121.42363	23.49222	978851.011	JSUI
121.37138	23.53160	978863.458	JPEI
121.30113	23.34093	978841.811	YULI
121.35889	23.34108	978849.153	JPIN
121.27990	23.14189	978814.496	AG2b
121.11871	23.13295	978759.943	AG03
121.16614	22.94218	978820.502	ERPN

四、台灣東部地質堅硬，重力量測成果穩定，而西部則是以較軟之地質，在重力實測結果有很明顯之不同，而台灣造山運動目前以AG3最為明顯，期望能有更多的數據來證明之前成果。

五、利用超導長期量測所得之重力數據，來求得各分潮之頻譜來代替全球模式，求得更精確之絕對重力值。

六、分析歐亞大陸板塊及菲律賓海板塊在經過數年之變化情形，利用實測數據來求得之間的相對關係。

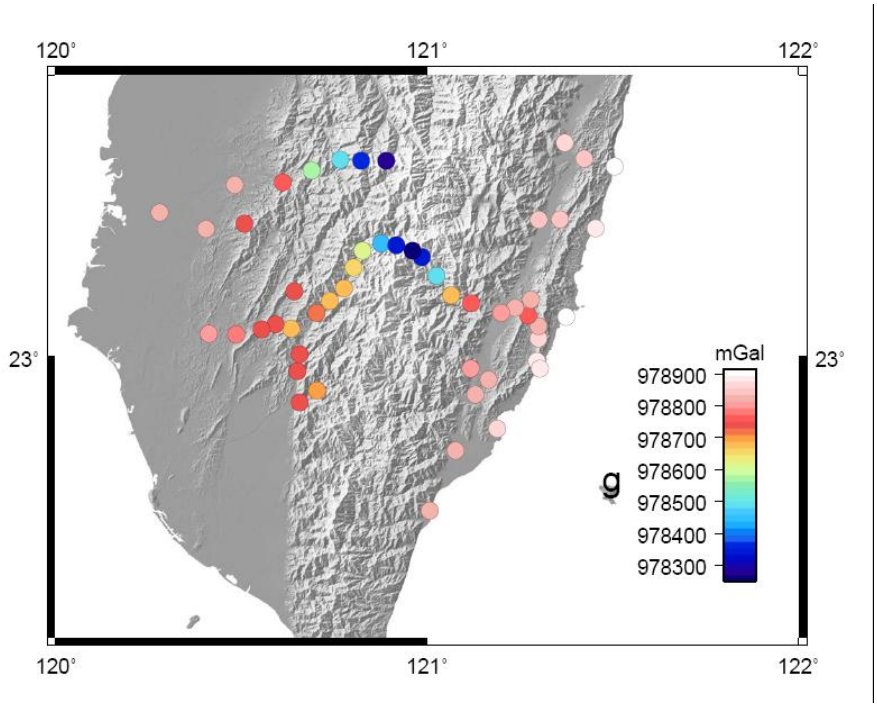

圖9 2008年相對重力數據展圖。可見重力值與監測站高程的關係。

對於參與之工作人員，可經由台灣與法方的互相交流提升台灣在重力相關領域中，各改正量及影響成因有更進一步的認知，結合台灣實測數據分析之能力及法國方面對地質環境意義之解釋，培養優秀之人材，經過長期的合作對台灣發展重力技術研究及提升有非常重要的幫助。

6.發表文獻

Article

M. Mouyen, F. Masson, C. Hwang, CC. Cheng, R. Cattin, CW. Lee, N. Le Moigne, J. Hinderer, J. Malavieille, R. Bayer, B. Luck, Expected temporal Absolute Gravity change across the Taiwanese Orogen, a modeling approach, Journal of Geodynamics, in press, 10.1016/j.jog.2009.09.004

Oral presentations

M. Mouyen, F. Masson, C. Hwang, C.-C. Cheng, C.-W. Lee, R. Kao, N. Hsieh, Four Years of Absolute Gravity in the Taiwan Orogen (AGTO), accepted for oral presentation at AGU Fall Meeting 2009, San Fransisco, USA, 14th-18th of December 2009.

F. Masson, M. Mouyen, C. Hwang, C.-C. Cheng, C.-W. Lee, R. Kao, N. Hsieh, Absolute gravity contribution to the Taiwanese orogenesis study, Colloque G2, Strasbourg, France, 18th-20th of November 2009.

F. Masson, M. Mouyen, C. Hwang, CC. Cheng, CW. Lee, J. Hinderer, N. Le Moigne, J. Malavieille, R. Bayer, R. Cattin, Study of the Taiwanese Orogen from Absolute Gravity Data, ETS 2008, Jena, Germany, 1st-5th of September 2008.

Poster presentation

F. Masson, M. Mouyen, C. Hwang, CC. Cheng, CW. Lee, N. Le Moigne, J. Hinderer, R. Cattin, B. Luck, R. Bayer, J. Malavieille, Study of the Taiwanese Orogen from Absolute Gravity Data : The AGTO project, AGU Fall Meeting 2008, San Fransisco, USA, 15th-19th of December 2008.

7. 參考文獻

黃金維、李瓊武、彭淼祥、鄭景中、高瑞其、謝文祺，國家重力基準站結案報告，2009年6月

張為民、王勇、許厚澤、張赤軍、郝興華、劉明，用FG5 絶對重力儀檢測青藏高原拉薩點的隆升，科學通報第45卷第20期，2000年10月

蔡義本、王乾盈等，政府科技發展領域策略規劃報告，陸、地球科學領域，民93

侯進雄、陳建良、王菁穗、謝中敏、鍾璋、鍾令和、陳彥甫，台灣西南地區地表斷層監測之近況與成果，經濟部中央地質調查所，2004年10月

Angelier, J. (1990). Geodynamic Evolution of the Eastern Eurasian Margin, Tectonophysics 183(1-4):special issue 362 pp.

Chapple, W. (1978), Mechanics of thin-skinned fold-and-thrust belts. *Geol. Soc. Am.* Bull. 89, 1189-1198.

Dahlen, F., A., Suppe, J., Davis, D. (1984), Mechanics of fold-and-thrust belts and

accretionary wedges: cohesive Columb *theory. J. Geophys. Res.* 89 (B12), 10,087-10101.

Davis, D. Suppe, J., Dahlen, F. (1983), Mechanics of fold-and-thrust belts and accretionary wedges. *J. Geophys. Res*. 88(B2), 1153-1172.

Hung, J., Wiltschko (1999), D.V., Lin, H.C., Hickman, J.B., Fang, P. and Bock, Y., Structure and motionof the southwestern Taiwan fold and thrust belt. TAO, v.10, no. 3, 543-568.

Hwang C, Hwang LS (2002) Use of geoid for assessing trigonometric height accuracy and detecting vertical land motion, Journal of Surveying Engineering, ASCE, 128 (1), pp. 1-20.

Koch, KR (1987) Parameter Estimation and Hypothesis Testing in Linear Models, Springer, Berlin.

Kao, H. and W.-P. Chen (2000). The Chi-Chi earthquake sequence: active, out-of sequence thrust faulting in Taiwan. Science 288: 2346-2349.

Malavieille, J. and Trullenque, G. (2007), Consequences of Continental Subduction on forearc basin and accretionary wedge deformation in SE Taiwan : insights from analogue modeling. : Tectonophysics, v. online, p. doi : 10.1016/j.tecto.2007.11.016.

Okada, Y.（1985）：Surface deformation due to shear and tensile faults in a half-space, Bull. Seism. Soc. Am., 75, 1135-1154.

Okada, Y.（1992）：Internal deformation due to shear and tensile faults in a half-space, Bull. Seism. Soc. Am., 82, 1018-1040.

Simoes, M. and Avouac, J.P. (2006) investigating the Kinematics of mountain building in Taiwan from the spatiotemporal evolution of the foreland basin and western foothills. J. Geophys. Res., 111, B10401.

Teng, L. S. (1990). Geotectonic evolution of late Cenozoic arc-continent collision in Taiwan. Tectonophysics 183: 57-76.

Won, I.J. and Bevis, M.G. (1987) Computing the gravitational and magnetic anomalies due to a polygon: Algorithms and Fortran subroutines. Geophysics, 52, 232-238.

Wu, F.T., R.-J. Rau, and D. Salzberg (1997), Taiwan orogeny: thin-skinned or lithospheric collision? Tectonophysics, 274, 191-220.

Yu SB, Hsu YJ, Kuo LC, Chen HY, Liu CC (2003) PS measurement of postseismic deformation following the 1999 Chi-Chi, Taiwan, earthquake , JOURNAL OF GEOPHYSICAL RESEARCH-SOLID EARTH 108 (B11): Art. No. 2520.

出 國 結 案 報 告 書

European Geosciences Union 2009

經　　費　　來　　源：　利用重力及 GPS 觀測台灣造山運動
97-2116-M-009-001-

出　　差　　人：黃金維

出　　國　　期　　間：2009.4.19-20095.4.24

出　　國　　地　　點：Vienna, Austria

中 華 民 國 98 年 4 月

一、　目的

二、　EGU2009 會議過程

三、　結論與建議

四、　攜回資料名稱與內容

一、 目的

The 2009 General Assembly of the European Geosciences Union (EGU) is held at the Austria Center Vienna (ACV) in Vienna, Austria, from 19 - 24 April 2009. The assembly is open to the scientists of all nations. The purpose of attending this meeting to present two papers: (1) Results from two years superconducting gravity observations in Taiwan, and (2) Multi-altitude airborne gravity for geoid determination: unification of Taiwan of height datum between and its offshore islands. I also met Dr David Crossley and J Hinderer of GGP and several other scientists to discuss the geoid and superconducting gravity research in Taiwan.

二、 EGU2009 會議過程

The 2009 meeting of European Geosciences Union was held in Vienna, Austria, April 19-24, 2009. The number of abstracts submitted to this meeting is over 12,000 and the number of attendees is about 10,000. The attendees are from all over the world, covering more than 60 countries. The scientific program includes such disciplines as atmosphere, space physics, geodesy, geology, planetary science, hydrology, and oceanography. I presented (1) Results from two years superconducting gravity observations in Taiwan, and (2) Multi-altitude airborne gravity for geoid determination: unification of Taiwan of height datum between and its offshore islands in Session G13 and G11. A number of useful comments were given to this paper. Many scientists show their interest in cooperation with Taiwan on and superconducting and airborne gravity research.

This meeting brought attention to methods for warning such disastrous events as soil erosion, flooding, land slide and volcano eruption. It appears inter-disciplinary methods are appealing and are trends for the future.

A significant amount of papers about precise orbit determination (POD) and gravity determination from GOCE (launched March 16, 2009) were presented in this meeting. Time-varying gravity from GRACE and its interpretations are also hot subjects of discussions.

三、 心得與建議

1. Gravity research is very active in Europe. Their techniques and theories are more sophisticated than those in Taiwan
2. Taiwan should put more resource in gravity research in order to compete with other nations

四、 攜回資料名稱及內容

論文摘要集光碟片 NASA、ＥＳＡ，CNES, NOAA 等研究成果書面及光碟片數份、其他論文宣讀及海報投影片十餘份等。

Results from parallel observations of superconducting and absolute gravimeters and GPS at the Hsinchu (HS) station of GGP, Taiwan

Cheinway Hwang[1], Ricky Kao[1,2], Ching-Chung Cheng[1], Jiu-Fu Huang[1,3], Chiung-Wu Lee[2] , and Tadahiro Sato[4]

[1] Department of Civil Engineering, National Chiao Tung University, 1001 Ta Hsueh Road, Hsinchu 300, Taiwan

[2] Dimensional Measurement Lab., Measurement Standards & Technology Div., CMS/ITRI, No. 321, Sec. 2 Kuang Fu Rd., Hsinchu 300, Taiwan

[3] Ministry of Interior, 5 Syujhou Rd., Jhongjheng District, Taipei 100, Taiwan

[4]Research Center for Prediction of Earthquakes and Volcanic Eruptions, Tohoku University, 6-6 Aza-Aoba, Aramaki, Aoba-ku, Sendai, 980-8578, Japan

Corresponding author:

Cheinway Hwang

Department of Civil Engineering, National Chiao Tung University, 1001 Ta Hsueh Road, Hsinchu 300, Taiwan

Email: cheinway@mail.nctu.edu.tw

20 Fax: +886-3-5716257

21 WWW: http://space.cv.nctu.edu.tw

22

Abstract

The Hsinchu (HS) superconducting gravimeter (SG, serial No. T48) station is a newly established site in the Global Geodynamics Project (GGP). Simultaneous observations of T48, three FG5 absolute gravimeters and GPS at four stations are studied. GPS shows few mm $year^{-1}$ of horizontal and vertical motions around HS. The calibration factor and drifting rate of T48 are -75.96±0.07 μgal V^{-1} and 0.2±0.7 μgal $year^{-1}$ (1 μgal = 10^{-8} m s^{-2}). Both the SG and absolute gravity records contain trends of about 2-3 μgal $year^{-1}$. The ocean tide gravity effects (OTGEs) were estimated from NAO.99b, FES2004 and CSR4.0, and their amplitudes agree with the SG observations at the sub-μgal level, but their phases differ from the observations up to 10º. The Newtonian effect of ocean tide contributes 20% to the total OTGE at HS, and it is larger at islands in the Taiwan Strait. The inelastic body tide model of DDW is more consistent with the SG observations than the elastic model. Modeled gravity-atmosphere admittances based on an exponential distribution of air mass explain well the observed admittances. The average gravity-atmosphere admittance during typhoons is 30% larger than that in a non-typhoon time. A list of co-seismic gravity changes from T48 caused by earthquakes over 2006-2007 is given for potential studies of fault parameters. The modeled effects of atmospheric pressure, ground water, soil moisture, and polar motion explain the FG5 observed gravity trend

to 1.1 μgal year^{-1}. Seasonally, the groundwater-induced gravity change contributes the most to the SG residual gravity, but its phase leads the latter by 63 days.

Keywords: absolute gravimeter, atmosphere, earthquake, GPS, superconducting gravimeter

1. Introduction

In March 2006, a single-sphere superconducting gravimeter (SG), serial number T48, was installed at Tunnel B of Mt. 18-Peak in the Hsinchu City, Taiwan. T48 is manufactured by GWR and has a nominal sensitivity of one ngal and a stability of few μgal $year^{-1}$ or better (1 ngal =10^{-11} m s^{-2} ; 1 μgal = 10^{-8} m s^{-2}). The Hsinchu SG station is now included in the SG network of the Global Geodynamics Project (GGP, http://www.eas.slu.edu/GGP/ggphome.html). The latitude, longitude and elevation of HS are 24.79258ºN and 120.98554ºE and 87.6 m, respectively. The scientific objectives and related issues of GGP, in particular GGP's role in the Global Geodetic Observing System (GGOS), are detailed by Hinderer and Crossley [2004] and Forsberg et al. [2005], and will not be elaborated here. Hereafter we will use the abbreviation HS to represent the Hsinchu SG station. Also, a second SG –T49 at HS is under test, but its result will not be reported here. Several meteorological sensors, a seismometer, a continuous GPS station and a groundwater monitoring well are deployed to monitor environment-induced gravity changes. Also, HS is about 8.6 km from the Taiwan Strait, where the average depth is 80 m and the ocean tide amplitude and phase are rapidly varying [Jan et al., 2004]. Taiwan, like many other regions in the western Pacific, is prone to attacks from such hazards as landslide, typhoon and earthquake. Installed at a proper location, a SG may be used to monitor man-made

and natural hazards.

In addition to supplying SG data to users interested in the targeted research subjects listed in GGP and GGOS, HS offers some extra features. HS is the closest station to the Tropic of Cancer in GGP and will be most sensitive to gravity change due to the motion of the earth's inner-core in the summer solstice, so that the SG data here are the best for testing the universality of free-fall [Shiomi, 2006]. Because of the short distance to shallow waters (8.6 km to the Taiwan Strait in the west), and the medium distance to deep waters (about 100 km to the Pacific in the east), the SG data at HS can be useful for studying the Newtonian effect and the loading effect of ocean tide. SG data at HS will enable the detection of non-linear ocean tides originating from the Taiwan Strait [Boy et al., 2004; Khan and Høyer, 2004]. A typhoon is an extremely low pressure system with abundant precipitating waters on the surface and in the air. Typhoons pass through Taiwan and the seas near this island from April to November, and create large gravity variations that are easily detectable at HS and can be used to investigate gravity change caused by atmospheric pressure change, including the effects originating from attraction, loading and inverted barometer [Boy et al., 2003; Hinderer and Crossley, 2004; Rccardi et al. 2007]. Finally, the co-seismic gravity change at HS due to a nearby earthquake will help to validate the fault parameters associated with the earthquake [Imanishi et al., 2004]. Real-time data of typhoons and earthquakes around Taiwan can be assessed at the Central

Weather Bureau of Taiwan (http://www.cwb.gov.tw).

With more than 2 years of SG data available at HS (from March 2006 to present), the objective of this paper is to present results on the quality assessment of the HS SG data and the applications of such data to selected problems. The geological settings and the regional tectonic motion around HS, based on previous geophysical explorations and continuous GPS observations, will also be presented. The calibration factor and the drifting rate of T48 will be estimated from parallel observations of absolute and SG gravity values, and these are two crucial parameters of T48 that must be taken into account when using the SG data at HS. The absolute gravity measurements were collected by three FG5 gravimeters from Taiwan and France. We will also employ standard models to account for the gravity changes due to atmosphere, groundwater, soil moisture and polar motion, which help to explain the origins of gravity changes obtained from FG5 and SG observations at HS.

2. Geological setting and GPS-derived regional tectonic motion

As shown in Figure 1, HS lies south of an alluvium created by two major rivers in Hsinchu. There are three non-active faults near HS. The Hsinchu Fault is within few hundreds of m to HS and is a normal fault lying in the west-east direction with a total length of 9 km. The latest movement of the Hsinchu Fault occurred some 100,000 years ago (Central Geological Survey of Taiwan, http://www.moeacgs.gov.tw), and it is expected

105 that there will be no immediate threat of large ground movement and earthquake at HS due
106 to this fault. HS is at the foot wall of the Hsinchu Fault and is situated on the "Toukeshan
107 formation" that has a distinct geological structure from that of the alluvium to the north.
108 The alluvium is fan-shaped and contains several soil layers. Figure 2 shows a cross-section
109 of the alluvium (Figure 1). The depths of the layer with shallow groundwater range from
110 10 m to 40 m. Below this surface layer lies several layers composed of gravel and fine sand
111 that can store groundwater. The amount of groundwater in these layers varies with rainfall,
112 which is largely brought by monsoons and typhoons. As such, the seasonal or shorter
113 time-scale changes of groundwater over the alluvium will create gravity variations at HS,
114 and will be discussed later in this paper.

115 Compared to the eastern coast of Taiwan, the western coast of Taiwan is relatively
116 quiet in terms of seismic activity. About 75% of earthquakes in Taiwan happen in the
117 eastern coast, and 25% in the western coast (Central Geological Survey of Taiwan). Based
118 on the GPS measuring results and a viscoelastic earthquake cycle model of Johnson et al.
119 [2005], the horizontal rates of plate motion in southeastern Taiwan are about 7-8 cm $year^{-1}$,
120 while the horizontal rates in the rest of Taiwan are few mm $year^{-1}$ to few cm $year^{-1}$. In this
121 paper, we used GPS data from four continuous GPS stations (Figure 1), spanning almost
122 the same time period as that of the HS SG data, to study the regional tectonic motion
123 around Hsinchu. Station HCHM is located on the summit of Mt. 18-Peak and is regarded

124 as a co-located station with HS. Station TCMS is in the International GPS Service (IGS)
125 network. Station SHJU is co-located with the Hsinchu tide gauge station. Using the IGS
126 precise GPS orbits (http://igscb.jpl.nasa.gov/) and the Bernese 5.0 software [Beutler et al.,
127 2007], daily coordinates of the four GPS stations were determined and their variations are
128 given in Figure 3. In general, all GPS stations show a consistent southeastward motion at a
129 speed of about 1- 2 cm year^{-1}, and the pattern of horizontal motion in Figure 3 is similar to
130 that given by Johnson et al. [2005]. Unlike the vertical motion, a localized and uniform
131 horizontal motion will not create a significant mass change leading to gravity change.

132 The vertical motions at the four GPS stations range from -3.5 to 0.5 mm year^{-1}.
133 TCMS and NCTU are several hundreds of m from HCHM and are located on the top of a
134 building. These two stations have been installed for over 10 years. Therefore, the
135 subsidence of the buildings will not contribute to the vertical rates detected by GPS over
136 2006-2008. The SHJU tide gauge station, installed in 2004, is situated at the Hsinchu
137 fishing harbor. Again the platform housing the SHJU tide gauge should be stable by 2006.
138 The vertical rate of HCHM (also HS) is 0.5±0.3 mm year^{-1}. Since there is neither major
139 man-made structure nor groundwater extraction near HCHM, the vertical motion at
140 HCHM (and therefore at HS) should be of tectonic origin. Furthermore, the vertical rate of
141 HCHM (at the foot wall) relative to TCMS (at the hanging wall) is 0.2±0.4 mm year^{-1},
142 which shows that the relative vertical displacement between the foot wall and the hanging

143 wall of the Hsinchu Fault is small.

144

145 **3. Parallel absolute and superconducting gravimeter observations**

146 **3.1 Calibration factor of T48**

147 It is necessary to determine a calibration factor of T48 that converts the raw SG
148 readings to readings in gravity. We determined an optimal calibration factor of T48 using
149 parallel observations of T48 and a FG5 absolute gravimeter (serial No. 231). The pillars
150 for T48 and FG5 are separated by about 1 m only. This method has been demonstrated by
151 Francis et al. [1998], Imanishi et al. [2002] and Tamura et al. [2005]. In total, 18 sessions of
152 parallel observations were collected. The following model is adopted for the determination
153 of the calibration factor:

154

155 $$g(t) = f_c V(t) + b - st \qquad (1)$$

156

157 where f_c is the calibration factor, b is an offset , s is the trend of T48 and g and V are
158 readings from FG5 and T48, respectively. Given the observations (g and V), the standard
159 least-squares technique is used to compute f_c, s and b. FG5 and T48 sense the same
160 gravity effects of solid earth tide and ocean tide, as well as any other time-varying
161 gravity effects, to produce gravity variations, which are exactly what we need for

162 determining the calibration factor. Before the least-squares solution, the outliers in the
163 T48 and FG5 data, which occur mostly during heavy rainfall, earthquakes and abrupt
164 changes of air pressure due to typhoons, were removed. As an example, Figure 4 shows the
165 T48 and FG5 data for calibration from the session of June 20, 2006 – July 2, 2006. The
166 variations in the FG5 gravity readings are mainly caused by the body tide and are almost
167 linearly correlated with the SG readings in voltage (correlation coefficient 0.953). The
168 residuals of FG5 observations from the least-squares adjustment (raw FG5 gravity values
169 minus fitted gravity values) follow the normal distribution, suggesting that the linear model
170 in Eq. (1) is adequate, and the estimated parameters are unbiased.

171 Table 1 lists the 18 parallel sessions and some useful information about the FG5
172 observations. Using all data from the 18 sessions, we obtained a calibration factor of
173 -75.96±0.07 μgal V^{-1} for T48. The trend *s* of T48 is 1.41±0.09μgal $year^{-1}$. Note that this
174 calibration factor (-75.96 μgal V^{-1}) was determined using all FG5 and T48 observations
175 simultaneously in one least-squares solution, rather than the average of the individual
176 calibration factors from the 18 sessions in Table 1. A calibration factor based on just one
177 session in Table 1 is considered less reliable. The standard error (0.07 μgal V^{-1}) is smaller
178 than 0.1 μgal V^{-1}, which is in general an acceptable value in the SG community [Tamura et
179 al. 2005]. The uncertainty in the calibration factor is largely caused by the random errors in
180 the FG5 observations. As mentioned before, HS is only 8.6 km from the sea, so the set

181 scatters of FG5 observations (from 1.3 to 4.1 μgal; Table 1) are larger than what would be
182 expected at a "quiet" station, where a typical set scatter is below 1 μgal. The calibration
183 factor of T48, to be published on the GGP web site, will be constantly improved as more
184 parallel FG5 and T48 observations are available in the future. Since the calibration factor of
185 T48 obtained in this paper has already been very precise, we expect only a minor change in
186 future updated values.
187
188 **3.2 Drift of T48**
189 The drift of a superconducting gravimeter will lead to a false interpretation of the
190 long-term gravity change at the SG site. Figure 5 shows the parallel FG5 and SG
191 observations from 2006 to 2008, with the solid tide and ocean tide gravity effects and
192 anomalous values removed. Some of the gravity values were collected by FG5 No. 224
193 (from Taiwan) and 228 (from France) when FG5 No. 231 (from Taiwan) was on the field
194 work. These two time series of gravity, sampled at different time intervals, show a
195 dominant annual cycle and an increasing trend. A gravity measurement from FG5 or T48,
196 $g(t)$, can be modeled as
197
198 $$g(t) = g_0 + \dot{g}t + c\cos wt + d\sin wt + e(t) \quad (2)$$
199

where t is time, g_0 is a constant, $\dot{g}$ is the linear change rate, c and d are the coefficients of the annual cycle, w is the annual frequency, and e is the measurement noise. Least-squares estimations were then employed to determine the four parameters in Eq. (2). The amplitude and phase were determined as $\sqrt{c^2+d^2}$ and $\tan^{-1}(d/c)$. As a result, the amplitudes of the annual cycle from FG5 and T48 are 5.9 and 6.3 μgal, and the phases are -22.9º and -26.1º. The difference in phase is partly due to data errors and partly due to the two different ways of sampling FG5 and SG measurements. The measurements of SG were almost continuous (sampling rate is 1 HZ) from March 2006 to present, but the measurements of FG5 were taken at the times given in Figure 5, and each FG5 gravity value was the average over several drops. The linear change rates from FG5 and T48 are 2.2±0.7 and 2.4±0.2 μgal year^{-1}. If we assume that the rate obtained by the FG5 gravimeters is a true rate of gravity change, the instrumental drift of T48 is estimated to be at a rate of 0.2±0.7 μgal year^{-1}. Note that this drifting rate (0.2 μgal year^{-1}) is estimated using the absolute gravity observations (serial No. 224, 228, and 231) from three FG5 absolute gravimeters. It differs from the trend (1.4 μgal year^{-1}) estimated in Section 3.1. This is explained by the fact that the trend in Eq. (1) may also absorb other un-modeled effects in the determination of the calibration factor and may not truly reflect the drift of T48.

4. Tidal analysis and observed tide

4.1 Preprocessing of the observed SG data

Before the tidal analysis, using the software "TSOFT" provided by the International Center for Earth Tides (ICET, http://www.astro.oma.be/ICET/), the SG data of T48 were de-spiked, filtered and decimated to hourly records for spectral analysis. Figure 6 shows the spectrum of the raw SG gravity records. As expected, we observe the six leading tidal components of M_2, K_1, S_2, O_1, N_2 and P_1 (in decreasing order of amplitude). Note the distinct signal component labeled M_3 in Figure 6 at a frequency of about 2.9 cycle day^{-1}, which is due to the M_3 ocean tide modulated by the complex bathymetry and coastal lines around the Taiwan Strait. This shows that, as pointed out by Hinderer and Crossley [2004], and Boy et al. [2004], SG provides interesting and important data to study non-linear tides over such a shallow-water area as the Taiwan Strait.

4.2 Tidal analysis

We compared the two computer programs ETERNA [Wenzel, 1996] and BAYTAP-G [Tamura et al., 1991] for tidal analysis. Tables 2 and 3 summarize the amplitude factors and phases along with the standard (formal) errors for the

238 short-period tides obtained by ETERNA and BAYTAP-G, respectively. A phase
239 shown in Table 2 and 3 is given as the phase difference from the equilibrium body
240 tide whose amplitude changes with the astronomical argument of each tidal
241 constituent. The standard errors in Tables 2 and 3 suggest that the estimated
242 amlitudes and phases are statistically meaningful. The tidal parameters obtained from
243 the two computer programs are quite consistent. As expected, the standard errors
244 increase with the tidal periods. The M_2 wave, the most dominant component in the
245 gravity time series, has the least standard error in both amplitude factor and phase.
246 The phase of ψ_1 constituent shows a large formal error exceeding 1º, which may be
247 reduced when a longer SG record than 2 years is available for the analysis.

248 To reduce the analysis error due to the contamination of the effect caused by
249 atmospheric pressure changes, the pressure term was included in the tidal analysis as
250 a term to be estimated. By using the barometer data simultaneously obtained at HS
251 with the SG data, we obtained the gravity-atmospheric admittances of -0.340±0.003
252 and -0.355±0.003 μgal hPa^{-1} from ETERNA and BAYTAP-G, respectively. Although
253 the two computer programs ETERNA and BAYTAP-G are developed independently,
254 they produce gravity-atmosphere admittances consistent to 97%. These values
255 represent a mean value for the gravity-atmosphere of the HS SG that is averaged over
256 the two years. As we will discuss in Section 5, the gravity-atmosphere admittance

257 will vary with the spatial and temporal scales of the atmospheric pressure change.

258 **4.3 Ocean-tide gravity effect**

259 We model the ocean-tide gravity effect (OTGE) according to the Green's
260 function approach, which is represented by

261

$$262 \quad \Delta g = \frac{G\rho_w}{R^2}\iint \frac{h(\phi,\lambda)(p-u)}{(1+p^2-2pu)^{3/2}}\,ds - \rho_w \iint h(\phi,\lambda)K(\psi)ds \qquad (3)$$

263

264 where G is the Newtonian gravitational constant, ρ is the density of sea water, R is
265 the mean earth radius, h is tidal height (depending on latitude ϕ and longitude λ), ψ
266 is spherical distance, $u = \cos\psi$, $p = (R+H)/R$, $ds = R^2\cos\phi d\phi d\lambda$, and K is
267 Greens' function based on the loading love numbers of Farrell [1972]. The first and
268 second terms of the right-hand side of Eq. (3) represent the effects of attraction and
269 loading, respectively. The detail of our OTGE model and software development is
270 given by Huang et al. [2008]. Note that the Newtonian (attraction) effect depends on
271 station height H through variable p.

272 In the Taiwan Strait, the amplitude of the M_2 ocean tide increases toward the
273 central part of the Strait and it reaches a maximum (about 2.2 m) at a latitude about
274 24ºN, and then decreases almost linearly northwards to the East China Sea and
275 southwards to the South China Sea. Also, there is a standing M_2 ocean tide near the

276 central Taiwan Strait [Jan et al., 2004]. As an example, the M_2 amplitudes at Keelung
277 (25.2ºN, near the East China Sea), Hsinchu (24.8ºN, near HS) and Pintung (22.0ºN,
278 near the South China Sea) are 0.6, 1.6 and 0.2 m, respectively.

279 SG observations can also be used to estimate OTGE, as carried out by Boy et al.
280 [2003]. This is achieved by removing an adopted body tide model from the SG data,
281 along with all the other known, well modeled signals, so that the residual SG gravity
282 values are assumed to contain the OTGE signal only. However, such an estimated
283 OTGE will be highly dependent on the adopted body tide model. As an experiment,
284 we removed the DDW body tide of Dehant et al. [1999] from the raw SG gravity
285 records. The remaining gravity values were then used to estimate OTGE at HS by
286 ETERNA software. The estimated OTGE will be then called the "observed" OTGE.
287 Figure 7 shows the amplitudes of the "observed" OTGE at HS and the amplitudes of
288 the ocean tide at the SHJU tide gauge station (Figure 1). In the amplitude spectra of
289 Figure 7, six leading components are identified: O_1, P_1, K_1, N_2, M_2 and S_2. It is
290 interesting to note that the relative magnitudes of these constituents are different
291 between the OTGE and the ocean tide. For OTGE, the order is M_2, O_1, K_1, S_2, N_2,
292 and P_1, while for the ocean tide, the order is M_2, S_2, N_2, K_1, O_1, and P_1. For both the
293 ocean tide and its gravity effect, the M_2 component is dominant. For ocean tide, M_2
294 contributes 47% to the total signal, while for OTGE the M_2 contribution is only 23%.

295 In addition to M_3, several other non-linear tides are also present in Figure 7. The SG
296 observations at HS can be used to study non-linear tides in the Taiwan Strait, as was
297 done by Boy et al. [2004) for European shallow waters.

298 Table 4 compares the amplitudes and phases of OTGE from the observations
299 (T48) and from the NAO.99b [Matsumoto et al., 2000], FES2004 [Lyard et al., 2006]
300 and CSR4.0 [Eanes and Bettadpur, 1996] ocean tide models for 8 short-period waves.
301 Overall, the OTGE from the NAO.99b tide model agrees the best with the SG
302 observations in both amplitudes and phases of all tidal components. The model
303 assessment by Penna et al. [2007] at TWTF, a continuous GPS station in Taiwan
304 some 30 km north of HS, also shows that, compared to FES2004, the ground
305 displacements predicted with NAO.99b are more consistent with the GPS observed
306 displacements. The discrepancies in amplitude are at the sub-μgal order, except for
307 the M_2 from CSR4.0. Compared with the diurnal tides, the modeled phases of the
308 semi-diurnal tides show relatively large discrepancy, showing the complexity in the
309 variations of the semi-diurnal tides in the Taiwan Strait. Therefore, there is room for
310 improvement of the tide models listed in Table 4, especially in the phases of the
311 semi-diurnal tides.

312 Since HS is near the Taiwan Strait, the Newtonian gravity effect of the ocean
313 tide can be significant. Using the NAO.99b tide model, we find that at HS the loading

effect and the Newtonian effect of M_2 are 3.01 and 0.75 μgal, respectively. Thus the Newtonian effect contributes 20% to the total effect. As shown in Eq. (3) and demonstrated by Lysaker et al. (2008), the Newtonian gravity effect is height-dependent. As an example, Table 5 shows such a height-dependence at HS and Lulin for M_2. Station Lulin (latitude=24.47109ºN and longitude=120.88081ºE) will house the second SG (T49) of Taiwan, and is about 74.5 km to the Taiwan Strait and 60.7 km to the Pacific. At both HS and Lulin, the Newtonian effect increases with elevation, and this is due to an increasing vertical component of the attraction as the elevation becomes larger. Lulin is distant from the sea in comparison to HS (74.5 vs. 8.6 km to the Taiwan Strait), so the Newtonian effect at Lulin is less sensitive to elevation change than that at HS.

At a given SG station near the sea, the spatial variation of tidal height can be assumed to be linear. With this assumption and following the method for evaluating the innermost zone contribution of gravity anomaly to geoid [Heiskanen and Moritz 1985], one finds the near-zone Newtonian effect of ocean tide as

$$g_i = C\frac{Gs_0\rho h}{4\pi R} \tag{4}$$

where s_0 is the radius of the near-zone zone, C is the ocean/land ratio near the station.

333 s_0 is the maximum distance that a linear variation of tidal height around the station
334 holds. Based on the amplitude variation of M_2 in the Taiwan Strait [Jan et al. 2004],
335 s_0 is about 10 km. Thus, for a station near the sea, the Newtonian effect is
336 proportional to the tidal height. Using the integrations in Eq. (3) and the NAO.99b
337 tide model, the largest Newtonian effect of ocean tide is found to be near Matzu,
338 which is an island in northwestern Taiwan Strait and offshore mainland China. For
339 example, at a permanent GPS tracking station on this island that is 500 m from the
340 sea, the amplitudes of the M_2 tide for the loading and Newtonian effects are 6.07 and
341 5.33 μgal, respectively. This implies that for a gravity station on an island, the
342 Newtonian gravity effect of ocean tide is about the same as the loading effect.
343
344 **4.4 Comparison with theoretical body tide**
345 In order to demonstrate the uniqueness of the HS SG station at its latitude
346 (about 25ºN) and the effect of OTGE correction, we compare the observed (this study)
347 and the theoretical amplitude factors for selected waves in Table 6. The theoretical
348 amplitude factors in Table 6 are given by the DDW model of Dehant at al. [1999] for
349 the elastic and inelastic earth, which are derived using the PREM earth model
350 [Dziewonski and Anderson, 1981]. The DDW amplitude factors are
351 latitude-dependent and can be expressed by

352

353
$$\delta_i^d = a_i^d + b_i^d \frac{\sqrt{6}}{4}(7\sin^2\phi - 3)$$
$$\delta_i^s = a_i^s + b_i^s \frac{\sqrt{3}}{2}(7\sin^2\phi - 1) \quad (5)$$

354

355 where ϕ is latitude, subscript *i* stands for tidal component, and superscripts *d* and *s*
356 stand for diurnal and semi-diurnal waves, respectively. The second terms in Eq. (5)
357 are the latitude-dependent terms contributing ~0.4% to the amplitude factors; see also
358 Torge [p. 398, 1989]. A "relative difference" in Table 6 is defined as the ratio between
359 the absolute difference (observation – model) and the observation. Three global
360 ocean tide models -NAO.99b, FES2004 and CSR4.0- were used to correct for the
361 OTGE in the SG data.

362 The amplitude factors corrected for OTGE agree better with the model factors of
363 DDW than the factors from the raw SG data. We observed in Table 6 that, in general,
364 the inelastic model of DDW agrees better with the observations of T48 than the
365 elastic model. Among three ocean models compared here, NAO.99b gives the
366 corrected amplitude factors which are most consistent with the factors expected from
367 the theory. In this case, if we take the mean value for the six major tidal constituents
368 having an amplitude exceeding 10 μgal (i.e. K1, O1, P1, N2, M2, and S2), the
369 relative difference for the inelastic model is smaller by about 22 % than that for the

370 elastic model, i.e. ratio of (0.602-0.470)/0.602. Moreover, for the mean of the same 6
371 constituents, we point out that the inelastic amplitude factor from the DDW (i.e.
372 1.1540) is systematically smaller by about 0.5 % than the observed one (i.e. 1.1595)
373 corrected by NAO.99b. Compared with the calibration error of 0.07% described in
374 Section 3, the difference of 0.5% is significant in the discussion of the tidal factor. It
375 is necessary to further improve the accuracy of the ocean tide correction to make
376 concrete conclusions on this, especially for the M_2 and O_1 constituents, which have
377 large amplitude and are far from the effect of the free core resonance (for example,
378 Wahr, 1981) appearing around the frequency of K_1 and ψ_1 constituents.
379

380 **5. Atmospheric pressure effect**

381 Using two years of SG and barometric data at HS, we obtained average
382 gravity-atmosphere admittances of -0.340±0.003 and -0.355±0.003 μgal hPa^{-1} from
383 ETERNA and BAYTAP-G, respectively. Note that the gravity-atmosphere admittance
384 is frequency dependent [Riccardi et al., 2007], but this subject is not pursued here. In
385 the following, we will interpret gravity-atmosphere admittances for various
386 atmospheric conditions, including typhoons. As shown by Ooe and Hanada [1982],
387 the distribution of air mass can be approximated by an exponential function, in which
388 the density change $\Delta\rho$ at a spot with a spherical angle θ_i to a given station is

389 represented by

390

391 $$\Delta\rho = \Delta\rho_0 e^{-|\theta_i|/\alpha} \quad (6)$$

392

393 where α is the horizontal scale (in the same units as the spherical angle) of the
394 atmospheric pressure change. In this paper, we adopt $\Delta\rho_0 = 1.225$ kg m^{-3} for HS. In
395 a normal case of slow and smooth pressure changes, the synoptic horizontal scale is
396 about 1000 km or more, and the temporal scale is about 3 days to 7 days. With the
397 approximation in Eq. (6), the analytical solution of the Newtonian attraction of the air
398 mass, expressed as admittance in μgal hPa^{-1}, can be written as [Ooe and Hanada,
399 1982]

400

401 $$\Delta g_A = -0.43[1 - \sum_{i=1}^{n}(\sqrt{\frac{1-\cos\theta_i}{2}} - \sqrt{\frac{1-\cos\theta_{i-1}}{2}})e^{-0.5|\theta_{i-1}+\theta_i|/\alpha}] \quad (7)$$

402

403 where n is the total number of segments of the coaxial rings centered at an
404 observation site. Also, the loading (elastic) effect of atmosphere can be estimated by
405 numerically convolving air mass and the loading Green's function as in the case of
406 the ocean tide loading effect (see Eq. (3)). The oceans respond to atmospheric
407 pressure changes as an inverted barometer (IB) over wide frequency bands [Wunsch

408 and Stammer, 1997], and the observations indicate that this hypothesis is well
409 realized in the frequency band lower than about 0.1 cycle day^{-1} [Matsumoto et al.,
410 2006]. If the IB response is completely established, there will be no loading effect
411 due to atmospheric pressure changes over the oceans, while in the case of the
412 non-IB response (NIB), the same loading effect is expected on sea and land. To
413 compare the computations based on conditions of the IB and NIB, we used two
414 topographic maps of ETOPO2 on a $2' \times 2'$ grid for the oceanic area around Taiwan,
415 i.e., over a region covering 20ºN-30ºN in latitude and 116ºE-120ºE in longitude
416 (ETOPO2 is available from
417 http://www.ngdc.noaa.gov/mgg/fliers/01mgg04.html). A 0.5º×0.5º land masking
418 map as used in NAO.99b was employed. A computer code modified from "GOTIC"
419 [Sato and Hanada , 1984] was used.

420 Figure 8 shows the gravity-atmosphere admittances at HS for the cases of IB
421 and NIB. The dependency of the Newtonian and loading effects upon the horizontal
422 scale (α) is given in Figure 8. Figure 8 suggests that the difference in the
423 admittances between the cases of IB and NIB becomes evident at 1˚.This is due to
424 the fact that the loading effect decreases rapidly as the horizontal scale decreases.
425 The IB hypothesis is well established at the horizontal scales of 10º-12º. The
426 admittances due to the Newtonian atmospheric effects in the cases of IB and NIB

427 are nearly identical at all horizontal scales. As shown in Figure 8, the average
428 observed admittance of -0.350 gal hPa^{-1} at HS corresponds to the admittance
429 associated with ≈ 10º in the case of IB response. Although a rigorous treatment of
430 the Newtonian atmospheric effect should be based on a 3-dimensional density
431 model of atmosphere [Neumeyer et al., 2004; Llubes et al., 2004], especially for the
432 seasonal variations in the atmospheric pressure effect on SG observations, the
433 present computation indicates that the mean observed admittance over 2 years
434 mainly reflects the effect of pressure variations at the synoptic scale.

435 It turns out that the observed admittances during typhoons are far from the mean
436 admittance. A typhoon is a very low pressure system that might create a large gravity
437 change. In the western Pacific, a typhoon might occur anytime from April to
438 November. Table 7 lists the gravity-atmosphere admittances for the typhoons over
439 2006 - 2007 that caused anomalous gravity changes at HS. Some of the parameters of
440 the typhoons are also given in Table 7. The mean of these 8 admittances is -0.45 gal
441 hPa^{-1}, which is 30% larger than (in magnitude) the mean value of -0.35 gal hPa^{-1} at
442 Hs. This phenomenon can be explained in part by the horizontal scale of a typhoon
443 (Figure 8), and the temporal scale of the variation of a typhoon. In general, the
444 horizontal scale of a typhoon is only few degrees, which corresponds to a distance
445 range where the contribution of loading effect is very small. Moreover, the speed of

446 typhoon is typically 30 km hour^{-1} to 40 km hour^{-1}, which is far from the frequency
447 range where the IB hypothesis is well established. The combined effect of the small
448 horizontal scale and the fast motion of air will shift the admittance from -0.35 gal
449 hPa^{-1} to a value of about -0.43 gal hPa^{-1}, which is the lowest value obtained from the
450 model computation here.

451 In addition to the spatial and temporal scales that result in different admittances
452 for the typhoon and non-typhoon conditions, other factors may also affect the
453 admittance during a typhoon, for example, the actual density of the central part of a
454 typhoon. A typical Doppler radar image of typhoon (see, e.g., the real-time radar
455 images at Central Weather Bureau of Taiwan) shows that the precipitating water is
456 not evenly distributed within the effective area of a typhoon and the convection
457 within a typhoon can be asymmetric; see, e.g., Chou et al. [2008] and Li et al. [2008].
458 In particular, condensation of water vapour contained in the moist air normally occurs
459 at low altitudes. Flooding and increased soil moisture will also lead to additional
460 gravity changes. Therefore, the gravity changes due to typhoons detected at HS can
461 be used to validate models of density distribution within a typhoon system, e.g., the
462 model of Chou et al. [2008] that is based on three-dimensional variational data
463 assimilation (3DVAR) and the Advanced Microwave Sounding Unit (AMSU) data.

464

6. Co-seismic gravity change due to earthquake

HS is close to an active earthquake zone belonging to the ring of fire in the western Pacific. Near real-time records of earthquakes around Taiwan can be found at http://www.cwb.gov.tw/V5/seismic/quake.htm. An earthquake will introduce oscillations in the gravity records. Depending on the magnitude, depth and distance to HS, the oscillation may last from few minutes to few hours. Such oscillations are considered as anomalous records and are often excluded from such analyses as body tide and ocean tide gravity effects. Hidden in the oscillations is a permanent gravity change that is caused by mass change and surface dislocation. The detection of such a permanent gravity change will require the modeling of a step function before and after the earthquake [Imanishi et al. 2004). Following the method used by Imanishi et al. [2004], we used the T48 records to determine permanent gravity changes due to earthquakes around Taiwan in 2006 and 2007, which are listed in Table 8. As an example, Figure 9 shows the permanent gravity change at HS due to an earthquake on September 6, 2007. The magnitude of this earthquake is 6.6 and the depth is 54 km. Situated at the Pacific Ocean northeast of Taiwan, the earthquake's epicenter is at latitude=24.28º and longitude=122.25º , some 155 km from HS. The gravity change due to the co- and post-seismic deformations was theoretically studied (for example, Wang et al. [2006], Fu and Sun [2008]). Although we must carefully check the instrumental instability as a possible source to make the gravity offset shown in

484 Table 8 by comparing the observed offsets to the amplitudes and the directions which
485 are expected from the theoretical estimations and the GPS observations carried out at
486 HS and nearby sites to it. However, Table 8 can be used to validate the theoretical
487 models that estimate co- and post-seismic gravity changes, and therefore help to
488 refine the fault parameters associated with an earthquake. Furthermore, it is noted
489 that cumulative gravity offsets due to earthquakes will be a possible significant
490 source of the secular gravity rate changes at HS.
491

492 **7. Residual gravity change**

493 **7.1 Observations and models**

494 The observed residual gravity changes at HS were obtained from the raw SG gravity
495 records corrected for the effects of the body and ocean tides (Section 4). Several sources
496 contribute to the gravity changes at a given gravity station; a summary of all possible
497 sources is given by Torge [1989]. One source is atmospheric pressure change, whose
498 gravity effects at short temporal scales have been discussed in Section 5. Another source of
499 gravity change is groundwater. Depending on the spatial scale sought, the
500 groundwater-induced gravity change is often classified into local, regional and global
501 variations. For a precise modeling of the local groundwater effect, the local hydro-geology
502 data must be given. At HS, the basic scenario of the hydro-geological structure is given in

503 Figures 1 and 2, but far more details are needed to account for the hydrology-induced
504 gravity changes. The water table at HS alone cannot fully describe the distribution of
505 groundwater over the Toukeshan formation around HS and over the alluvium north of HS.
506 Furthermore, a soil moisture sensor is deployed right above Tunnel B that houses T48.
507 However, the soil moisture data collected here will not be representative of water
508 distribution in the unsaturated layers around HS. Despite these difficulties, preliminary
509 models to account for the residual gravity changes at HS due to non-geodynamic origin are
510 presented below.

511 (1) Atmospheric pressure effect (μgal)

512

513 $$\delta g_b = f_a (P_a - 1013) \quad (8)$$

514

515 where P_a is pressure in hPa, 1013 hPa is the standard atmospheric pressure at HS and f_a
516 is the gravity-atmosphere admittance. According to the result in Section 5, we set f_a =
517 -0.350 μgal hPa^{-1}.

518 (2) Groundwater effect (μgal)

519

520 $$\delta g_w = 0.42 P \delta H \quad (9)$$

521

where P is the porosity of soil in percentage and δH is groundwater level variation in m. We adopt P=10% as the optimal porosity for the Toukeshan formation (Section 2).

(3) Soil moisture effect (μgal)

$$\delta g_s = -0.42 H \delta P \tag{10}$$

where H is the depth of unsaturated soil layer and δP is the recorded soil moisture change in percentage . Here we adopt $H = 1$ m. The minus sign in Eq. (10) is due to the fact that T48 is housed in a tunnel beneath the unsaturated soil.

(4) Polar motion effect (μgal)

$$\delta g_p = 1.164 \times 10^8 \omega^2 R \sin 2\varphi (x_p \cos\lambda - y_p \sin\lambda) \tag{11}$$

where ϕ, λ are latitude and longitude, and x_p, y_p are polar motion components in radian , which are available from the International Earth Rotation Service (IERS, http://www.iers.org).

Figure 10 compares the observed (by T48) residual gravity changes and the modeled values at HS. Conclusions on the non-linear gravity changes based on Figure 10 are given below.

541 (1) At the time scales of hours to days, the largest contribution to the observed residual
542 gravity change is from the atmospheric pressure change. In fact, the analysis in Section
543 5 shows that the correlations between residual gravity change and atmospheric pressure
544 change at such short time scales are more than 90% in most cases. The episodic
545 changes of gravity due to groundwater have to do with sudden rainfalls. The soil
546 moisture also creates short-period gravity variations, but the pattern of variation is quite
547 irregular. There are no clear short-period gravity variations due to polar motions.
548 (2) The observed and modeled gravity changes all contain annual variations, but with
549 different amplitudes and phases. Table 9 lists these amplitudes and phases. The
550 amplitude of the groundwater gravity effect is the largest, followed by that of the
551 atmosphere gravity effect. The amplitudes of the soil moisture and polar
552 motion-induced annual gravity change are almost equal, and are 1/4 of the groundwater
553 gravity effect. Seasonally, the modeled gravity changes due to atmosphere and
554 groundwater lead the observed residual gravity by 110 and 63 days, while the modeled
555 gravity changes due to soil moisture and polar motion lag behind the observed ones by
556 about 12 days. Disagreements in amplitude and phase between observed gravity
557 change and hydrology-induced gravity change are very common, as shown by Boy and
558 Hinderer [2006] and Neumeyer et al. [2008] at selected GGP stations. In the case of HS,
559 exactly how and how long the aquifers under the alluvium (Figure 1) are filled and

560 drained are not clear, and these uncertainties contribute to the disagreement between
561 the observed and groundwater-induced gravity changes.
562 (3) Clearly the models in Eq. (8)-(11) have deficiencies, e.g., the 63-day phase difference
563 between the observed and groundwater-induced gravity changes. On the other hand,
564 the SG and FG5 observed gravity changes may be used to investigate such problems as
565 flow of groundwater and small-scale hydrological process; see, e.g., Jacob et al. [2008]
566 and Naujoks et al. [2008].
567
568 **7.2 Rate of gravity change at HS**
569 As shown in Section 3.2, the absolute and T48 gravity records all show a long-term
570 trend of gravity change at HS. The origins of the trend are now interpreted using the
571 modeled gravity changes given in Section 7.1, plus the vertical displacement given in
572 Section 2. The rates of the modeled gravity changes are listed in Table 10. The total rate
573 from these models is 3.3±0.8 μgal year^{-1}, compared to 2.2±0.7 μgal year^{-1} from the absolute
574 gravimeter measurements (Section 3.2). Therefore, the modeled rates cannot fully account
575 for the observed rate of gravity change. One source of the gravity change not accounted for
576 in Table 10 at HS is earthquakes around Taiwan. For example, the earthquake occurring on
577 September 6, 2007 created a gravity offset of 0.6 μgal, which contributes a rate of 0.3 μgal
578 year^{-1} to the total rate at HS over two years (Section 6). Other small earthquakes will also

579 create gravity changes that eventually add to the rate of gravity change at HS. Gravity
580 change due to sea-level rise will also contribute to the rate of gravity change recorded at HS.
581 An example of gravity change due to sea level rise over the Baltic Sea is given by Virtanen
582 and Makinen [2003]. At the global scale, a rising rate of 3.1 mm $year^{-1}$ in sea level, as
583 estimated from TOPEX/Poseidon and Jason-1 satellite altimeter data [Nerem et al., 2006],
584 will lead to a rate of 0.2 μgal $year^{-1}$ in gravity based on a simple Bouguer model for the
585 effect of oceanic water mass.
586

587 **8. Conclusions**

588 This paper summarizes the findings from the observations of a superconducting
589 gravimeter (T48), three FG5 absolute gravimeters (serial no. 224,228, and 231) and a
590 regional GPS network around HS. The main purpose of this work is to show some of T48's
591 critical parameters and its potential applications to such studies as SET, OTGE, typhoon
592 and earthquake. The area north of HS is a groundwater-rich alluvium that introduces
593 gravity variation at HS. A vertical site motion of 0.5±0.3 mm $year^{-1}$ at HS was found and is
594 not directly related to the movement of the Hsinchu Fault. Using the parallel FG5 and T48
595 observations, the calibration factor and the drifting rate of T48 were found to be
596 -75.96±0.07 μgal V^{-1} and 0.2±0.7 μgal $year^{-1}$, respectively. The observed drifting rate of
597 T48 is smaller than the nominal drift of few μgal $year^{-1}$ reported by the SG manufacturer.

598 The relative differences between the gravimetric amplitude factors determined with T48
599 (corrected by NAO.99b) and the model factors of Dehant et al. [1999] range from 0.05 to
600 3.93%. The OTGE model amplitudes and phases from the NAO.99b tide model agree the
601 best with the observations of T48. The Newtonian part contributes a significant portion to
602 OTGE (about 20% for M_2 at HS) at an ocean-side SG station such as HS. A density
603 distribution model of atmospheric pressure change based on an exponential function
604 predicts the gravity-atmosphere admittances that agree well with the observations. The
605 gravity-atmosphere admittances during typhoons are 30% larger than the mean.

606 The residual gravity from T48 shows a distinct annual cycle and a linear trend.
607 Four models of temporal gravity changes are used to explain the SG residual gravity, but
608 there exist a significant discrepancy between the observations of T48 and the model values.
609 Seasonally, the groundwater-induced gravity change leads the SG residual gravity by 63
610 days. The phases of the annual cycles from other sources deviate from that of the SG
611 residual gravity by tens of days to a few months. Both typhoons and earthquakes around
612 Taiwan created large gravity variations at HS. The SG records at HS are able to detect
613 co-seismic gravity changes around Taiwan, and the example given in this paper serves as
614 the beginning of the SG-earthquake research using the SG data at HS. In summary, with
615 the necessary information presented in this paper, the SG (T48) at HS has delivered data
616 that meet the quality standard and are ready to be used in a number of geodetic and

617 geophysical problems.

618

619 **Acknowledgements**

620 This study is supported by Ministry of the Interior and National Science Council, Taiwan,
621 Republic of China. Dr Horng-Yue Chen of Institute of Earth Sciences, Academia Sinica,
622 helped to compute the site displacements from GPS at Hsinchu. The comments of two
623 anonymous reviewers greatly improved the quality of this paper.

624

625 **References**

626 Beutler, G., H. Bock, E. Brockmann, R. Dach, P. Fridez, A. W. Gäde, U. Hugentobler,
627 A. Jäggi, M. Meindl, L. Mervart, L. Prange, S. Schaer, T. Springer, C. Urschl, and P.
628 Walser (2007), Bernese GPS Software Version 5.0, *Astronomical Institute*,
629 University of BERN, Switzerland.

630 Boy, J. P., M. Llubes, J. Hinderer, and N. Florsch (2003), A comparison of tidal ocean
631 loading models using superconducting gravimeter data, *J. Geophys. Res.*, *108*, Art
632 No. 2193, doi: 10.1029/2002JB002050.

633 Boy, J. P., M. Llubes, R. Ray, J. Hinderer, N. Florsch, S. Rosat, F. Lyard, and T. Letellier
634 (2004), Non-linear oceanic tides observed by superconducting gravimeters in Europe,
635 *J. Geodyn.*, *38*, 391-405.

636 Boy, J. P., and J. Hinderer (2006), Study of the seasonal gravity signal in superconducting
637 gravimeter data, J. *Geodyn*., *41*, 227-233.
638 Chou, C. B., C. Y. Huang, H. P. Huang, K. H. Wang, and T. C. Yeh (2008), The analysis of
639 typhoon structures using advanced microwave sounding unit data and its application
640 to prediction, *J. Appl. Meteor. Climatology*, *47*, 1476-1492, doi:
641 10.1175/2007JAMC1577.1.
642 Dehant, V., P. Defraigne, and J. M. Wahr (1999), Tides for a convective Earth. *J. Geophys.*
643 *Res*., *104*, 1035-1058.
644 Dziewonski, A. D., and D. L. Anderson (1981), Preliminary reference Earth model,
645 *Phys. Earth Planet. Inter*., *25*, 297-356.
646 Eanes, R., S. Bettadpur (1996), The CSR3.0 global ocean tide model: Diurnal and
647 Semi-diurnal ocean tides from TOPEX/POSEIDON altimetry, *CRS-TM-96-05*,
648 University of Texas, Centre for Space Research, Austin, Texas.
649 Farrell, W. E. (1972), Deformation of the earth by surface loads, *Rev. Geophys. Space Phys*.,
650 *10*, 761-797.
651 Forsberg, R., M. G. Sideris, and C. K. Shum (2005), The gravity field and GGOS, *J.*
652 *Geodyn*., *40*, 387-393, doi: 10.1016/j.jog.2005.06.014.
653 Francis, O., T. M. Niebauer, G. Sasagawa, F. Klopping, and J. Gschwind (1998),
654 Calibration of a superconducting gravimeter by comparison with an absolute

655 gravimeter FG5 in Boulder, *Geophys. Res. Lett.*, *25*, 1075-1078.

656 Fu, G. Y., and W. K. Sun (2008), Surface coseismic gravity changes caused by dislocations
657 in a 3-D heterogeneous earth, *Geophys. J. Int.*, *172*, 479-503, doi:
658 10.1111/j.1365-246X.2007.03684.x

659 Huang, J. F., C. Hwang, and S. Jan (2008), Modeling gravity effect of ocean tidal loading
660 around Taiwan: accuracy assessment using FG5 and superconducting gravity data,
661 *Western Pacific Geophysics Meeting*, AGU, July 29- Aug 1, 2008.

662 Heiskanen, W. A., and H. Moritz (1985), *Physical Geodesy*, reprint, Tech. University
663 Graz.

664 Hinderer, J., and D. Crossley (2004), Scientific achievements from the first phase
665 (1997–2003) of the Global Geodynamics Project using a worldwide network of
666 superconducting gravimeters, *J. Geodyn.*, *38*, 237-262.

667 Imanishi, Y., T. Higashi, and Y. Fukuda (2002), Calibration of the superconducting
668 gravimeter T011 by parallel observation with the absolute gravimeter FG5 #210 - a
669 Bayesian approach, *Geophys. J. Int.*, *151*, 867-878.

670 Imanishi, Y., T. Sato, T. Higashi, W. K. Sun, and S. Okubo (2004), A network of
671 superconducting gravimeters detects submicrogal coseismic gravity changes, *Science*,
672 *306*, 476 – 478, doi: 10.1126/science.1101875.

673 Jacob, T., R. Bayer, J. Chery, H. Jourde, N. Le Moigne, J. P. Boy, J. Hinderer, B. Luck,
674 and P. Brunet (2008), Absolute gravimetry monitoring of water storage variation in a
675 karst aquifer on the larzac plateau (Southern France), *J. Hydrol.*, *359*, 105-117.

676 Jan, S., C. S. Chern, J. Wang, and S. Y. Chao (2004), The anomalous amplification of M_2
677 tide in the Taiwan Strait, *Geophys. Res. Lett.*, *31*, L07308,
678 doi:10.1029/2003/GL019373.

679 Johnson, K. M., P. Segall, and S. B. Yu (2005), A viscoelastic earthquake cycle model for
680 Taiwan, *J. Geophys. Res.*, *110*, B10404, doi: 10.1029/2004JB003516

681 Khan, S. A., and J. L. Høyer (2004), Shallow-water loading tides in Japan from
682 superconducting gravimetry, *J. Geod.*, *78*, 245-250.

683 Li, Q. Q., Y. H. Duan, H. Yu, and G. Fu (2008), A high-resolution simulation of Typhoon
684 Rananim (2004) with MM5. Part I: Model verification, inner-core shear, and
685 asymmetric convection, *Mon. Weather Rev.*, *136*, 2488-2506, doi:
686 10.1175/2007MWR2159.1.

687 Llubes, M., N. Florsch, J. Hinderer, L. Longuevergne, M. Amalvict (2004), Local
688 hydrology, the Global Geodynamics Project and CHAMP/GRACE perspective:
689 some case studies, *J. Geodyn.*, *38*, 355-374 .

690 Lyard, F., F. Lefevre, T. Letellier, and O. Francis (2006), Modeling the global ocean tides:
691 modern insights from FES2004, *Ocean Dynamics*, *56*, 394-415.

692 Lysaker, D. I., K. Breili, and B. R. Pettersen (2008), The gravitational effect of ocean
693 tide loading at high latitude coastal stations in Norway, *J. Geod.*, *82*, 569-583.
694 Matsumoto, K., T. Takanezawa, and M. Ooe (2000), Ocean tide models developed by
695 assimilating TOPEX/POSIDON altimeter data into hydrodynamical model: A global
696 model and a regional model around Japan, *J. Oceanogr.*, *56*, 567-581.
697 Matsumoto, K., T. Sato, H. Fujimoto, Y. Tamura, M. Nishino, R. Hino, and T. Higashi
698 (2006), Ocean bottom pressure observation off Sanriku and comparison with ocean
699 tide models, altimetry, and barotropic signals from ocean models, *Geophys. Res. Lett.*,
700 *33*, L16602, doi: 10.1029/2006GL026706.
701 Naujoks, M., A. Weise, C. Kroner, and T. Jahr (2008), Detection of small hydrological
702 variations in gravity by repeated observations with relative gravimeters, *J. Geod.*,
703 *82*,543-553.
704 Nerem, R. S., E. Leuliette, and A. Cazenave (2006), Present-day sea-level change: A review,
705 *Comptes Rendus Geoscience*, *338***,** 14-15.
706 Neumeyer, J., J. Hagedoorn, J. Leitloff, and T. Schmidt (2004), Gravity reduction
707 with three-dimensional atmospheric pressure data for precise ground gravity
708 measurements, *J. Geodyn.*, *38*, 437-450.
709 Neumeyer, J., F. Barthelmes, C. Kroner, S. Petrovic, R. Schmidt, H. Virtanen, and H.
710 Wilmes (2008), Analysis of gravity field variations derived from

711 superconducting gravimeter recordings, the GRACE satellite and hydrological
712 models at selected European sites, *Earth Planets Space*, *60*, 505-518.
713 Ooe, M., and H. Hanada (1982), Physical simulations of effects of the atmospheric
714 pressure and the ground water upon gravitational acceleration and crustal
715 deformation, *Publ. Int. Lat. Obs. Mizusawa, No. 21*, 6-14. (in Japanese)
716 Penn, T. N., M. A. King, and M. P. Stewart (2007), GPS height time series: Short-period
717 origins of spurious long-period signals, *J. Geophys. Res.*, *11*, B02402, doi:
718 10.1029/2005JB004047.
719 Riccardi, U., J. Hinderer, and J. P. Boy (2007), On the efficiency of barometric arrays to
720 improve the reduction of atmospheric effects on gravity, *Phys. Earth Plant.*
721 *Inter.*, *161*, 224-242, doi: 10.1016/j.pepi.2007.02.007
722 Sato, T., and H. Hanada (1984), A program for the computation of oceanic tidal loading
723 effects "GOTIC", *Proc. Int. Conf. Earth Rotation and Terrest Refer. Frame*, 742-747
724 Shiomi, S. (2006), Geophysical test of the universality of free-fall, *Phys. Rev. D: Part.*
725 *Fields, 74*, 027101.
726 Tamura, Y., T. Sato, M. Ooe, and M. Ishiguro (1991), A procedure for tidal analysis with a
727 Bayesian information criterion, *Geophys. J. Int.*, *104*, 507-516.
728 Tamura, Y., T. Sato, Y. Fukuda, and T. Higashi (2005), Scale factor calibration of a
729 superconducting gravimeter at Esashi Station, Japan, using absolute gravity

730 measurements, *J. Geod., 78*, 481-488.

731 Torge, W. (1989), *Gravimetry*. De Gruyter, Berlin.

732 Virtanen, H., and J. Makinen (2003), The effect of the Baltic sea level on gravity at the

733 Metsahovi station, *J. Geodyn.*, *35*, 553-565.

734 Wahr, J. (1981), Body tides on an elliptical, rotating, elastic and oceanless earth, *Geophys. J.*

735 *R. Astr. Soc*., *64*, 677-704.

736 Wang, R. J., F. Lorenzo-Martín, and F. Roth (2006), PSGRN/PSCMP- a new code for

737 calculating co- and post-seismic deformation, geoid and gravity changes based on

738 the viscoelastic-gravitational dislocation theory, *Comput. Geosci*., *32*, 527-541.

739 Wenzel, H. G. (1996), The nanogal software: Earth tide processing package ETERNA 3.30.

740 *Bull. d'Inf Marées Terr.*, *124*, 9425-9439.

741 Wunsch, C., and D. Stammer (1997), Atmospheric loading and the oceanic "Inverted

742 Barometer'' effect, *Rev. Geophys*., *35*, 79-107.

743

744 **List of tables**

745 **Table 1:** Sessions of parallel superconducting (T48) and absolute (FG5) gravity
746 observations for determining the calibration factor of T48

Satring time of session (GMT)	Length (hour)	FG5 Set scatter (μgal)	Total uncer. (μgal)	Number of drops
6h, June 5, 2006	30	4.1	2.1	3479
1h, June 9, 2006	29	2.5	2.1	3500
6h, June 13, 2006	24	2.3	2.1	2807
2h, June 21, 2006	48	1.5	2.0	5716
3h, June 30, 2006	48	1.3	2.0	5746
5h, July 7, 2006	95	2.3	2.1	10772
9h, October 11, 2006	19	3.4	2.2	2224
6h, November 4, 2006	24	2.7	2.1	4109
3h, November 17, 2006	24	2.4	2.4	4713
8h, March 2, 2007	39	2.2	2.1	4668
7h, March 4, 2007	72	3.7	2.1	8427
12h, November 10, 2007	28	3.3	2.2	6123
9h, November 30, 2007	72	2.2	2.0	17242
0h, December 16,2007	72	1.7	2.0	17018
0h, January 2, 2008	24	2.5	2.1	5399
0h, January 7, 2008	72	2.0	2.1	16789
0h, February 6, 2008	48	3.1	2.1	11510
0h, February 21, 2008	72	1.8	2.1	16713

747

748

749 **Table 2:** Tidal analysis results by ETERNA

Wave	Amplitude (μgal)	Amplitude factor	Phase (º)
Q_1	5.649±0.008	1.2485±0.0018	-1.34±0.08
O_1	29.061±0.008	1.2298±0.0003	-2.28±0.02
M_1	2.251±0.007	1.2119±0.0036	-2.50±0.17
P_1	13.125±0.010	1.1939±0.0009	-2.74±0.04
S_1	0.317±0.014	1.2178±0.0541	2.54±2.55
K_1	39.145±0.009	1.1784±0.0003	-2.84±0.01
ψ_1	0.331±0.009	1.2712±0.0355	-5.38±1.60
$ø_1$	0.584±0.010	1.2348±0.0209	-0.96± 0.97
J_1	2.191±0.008	1.1791±0.0045	-3.36±0.22
OO_1	1.173±0.005	1.1544±0.0049	-2.51±0.24
$2N_2$	2.314±0.011	1.2232±0.0058	1.86±0.27
N_2	13.947±0.014	1.1773±0.0012	-3.40±0.06
M_2	71.452±0.014	1.1548±0.0002	-3.03±0.01
L_2	1.817±0.018	1.0388±0.0104	-0.81±0.58
S_2	33.093±0.014	1.1497±0.0005	-1.63±0.02
K_2	9.033±0.011	1.1550±0.0014	-1.59±0.07
M_3	1.203±0.003	1.0908±0.0024	-0.31±0.12

750

751 **Table 3:** Tidal analysis results by BAYTAP-G

Wave	Tidal amplitude (μgal)	Amplitude factor	Phase (º)
Q_1	5.646±0.017	1.2482±0.0037	-1.45± 0.17
O_1	29.056±0.016	1.2299±0.0007	-2.28± 0.03
M_1	2.239±0.011	1.2053±0.0060	-2.51± 0.29
P_1	13.117±0.016	1.1933±0.0015	-2.65± 0.07
S_1	0.309±0.004	1.1874±0.0142	-2.12± 0.69
K_1	39.149±0.014	1.1783±0.0004	-2.83± 0.02
ψ_1	0.309±0.004	1.1888±0.0157	-2.96± 0.76
$ø_1$	0.563±0.007	1.1896±0.0153	-2.85± 0.74
J_1	2.193±0.012	1.1801±0.0066	-3.34± 0.32
OO_1	1.176±0.007	1.1573±0.0068	-2.86± 0.34
$2N_2$	1.919±0.003	1.2247±0.0020	1.81± 0.09
N_2	13.947±0.005	1.1778±0.0004	-3.36± 0.02
M_2	71.435±0.005	1.1550±0.0001	-3.03± 0.00
L_2	1.831±0.006	1.0473±0.0033	-0.75± 0.18
S_2	33.057±0.004	1.1488±0.0001	-1.89± 0.01
K_2	9.031±0.003	1.1546±0.0004	-1.63± 0.02
M_3	1.206±0.002	1.0942±0.0018	-0.16± 0.10

752 **Table 4:** Amplitudes and phases of ocean-tide gravity effect at HS from T48
753 observations and from NAO.99b, FES2004 and CSR4.0 ocean tide models

Wave	T48	NAO.99b	FES2004	CSR4.0
M_2	3.82[a]	3.76	3.37	2.85
	-98.0[b]	-99.6	-91.8	-122.2
N_2	0.84	0.82	0.75	0.93
	-79.1	-76.7	-58.9	-56.5
S_2	1.12	0.95	0.87	0.82
	-110.5	-114.4	-86.4	-42.7
K_2	0.26	0.24	0.25	0.31
	-103.1	-108.0	-81.9	-30.4
K_1	2.38	2.40	2.15	2.47
	-54.2	-55.1	-51.1	-58.9
O_1	2.10	2.08	2.01	2.13
	-33.2	-30.8	-34.1	-30.6
P_1	0.78	0.78	0.71	0.82
	-53.0	-52.8	-53.1	-56.7
Q_1	0.45	0.44	0.41	0.48
	-17.4	-22.4	-23.8	-23.3

754 [a]amplitude in μgal, [b]phase in degrees

755

756

757

758 **Table 5:** The amplitude of the Newtonian effect of M_2 ocean tide as a function of
759 height at the SG stations of HS and Lulin

Height (m)	HS (μgal)	Lulin (μgal)
0	0.66	0.69
100	0.70	0.69
200	0.80	0.69
300	0.93	0.70
400	1.08	0.70
500	1.25	0.70

760
761

762 **Table 6:** Amplitude factors from T48 observations and the DDW model

Wave	Factor from theory		T48 corrected by NAO.99			T48 corrected by FES2004			T48 corrected by CSR4.0		
	elastic	inelastic	factor	elastic[a]	inelastic[a]	factor	elastic[a]	inelastic[a]	factor	elastic[a]	inelastic[a]
ψ_1	1.2344	1.2656	1.3153	6.15	3.78	1.3088	5.68	3.30	1.3200	6.48	4.12
$\o_1$	1.1672	1.1696	1.2175	4.13	3.93	1.2177	4.15	3.95	1.2186	4.22	4.02
OO_1	1.1547	1.1561	1.1556	0.08	0.043	1.1555	0.07	-0.05	1.1557	0.09	-0.03
K_1	1.1335	1.1355	1.1416	0.71	0.53	1.1420	0.74	0.57	1.1444	0.95	0.78
O_1	1.1527	1.1542	1.1661	1.15	1.02	1.1701	1.48	1.36	1.1646	1.02	0.89
N_2	1.1603	1.1617	1.1724	1.03	0.91	1.1500	-0.90	-1.02	1.1531	0.62	-0.75
P_1	1.1479	1.1493	1.1501	0.19	0.07	1.1541	0.54	0.42	1.1521	0.36	0.24
K_2	1.1603	1.1617	1.1640	0.32	0.20	1.1532	-0.62	-0.74	1.1304	2.65	2.77
Q_1	1.1527	1.1542	1.1379	-1.30	-1.43	1.1459	-0.59	-0.72	1.1308	-1.94	-2.07
M_2	1.1603	1.1617	1.1645	0.36	0.24	1.1564	-0.34	-0.46	1.1802	1.69	1.57
S_2	1.1603	1.1617	1.1623	0.17	0.05	1.1470	-1.16	-1.28	1.1278	2.88	3.01
M_3	1.0724	1.0734	1.0927	1.86	1.77	1.0926	1.85	1.76	1.0926	1.85	1.76

763 [a] relative difference in %

764 **Table 7:** Gravity changes due to typhoons and gravity-atmosphere admittances at HS

Typhoon	Date	Center pressure (hPa)	Category	Pressure change (hPa)	Gravity change (μgal)	Admittance (μgal hPa^{-1})
Chanchu	May 16,2006	960	2	11	5.5	-0.47
Bilis	July 12,2006	985	1	28	8.6	-0.45
Kaemi	July 23,2006	960	2	19	8.0	-0.43
Bopha	August 7,2006	992	1	4	1.5	-0.48
Shanshan	September 14,2006	940	2	7	3.0	-0.45
Wutip	August 8, 2007	992	1	5	2.2	-0.41
Sepat	August 16, 2007	925	3	23	8.5	-0.52
Krosa	October 4, 2007	940	3	35	12.5	-0.40

765

766 **Table 8:** Gravity shifts due to earthquakes around Taiwan at HS

Date	Distance (km)	Depth (km)	Magnitude of earthquake	Gravity shift (μgal)
April 1, 2006	214	9	6.2	1.19
April 15, 2006	223	17	6.0	-0.17
April 28, 2006	109	8	5.2	-0.61
July 28, 2006	170	49	6.0	1.01
August 27, 2006	197	145	6.0	0.00
October 12, 2006	181	44	5.8	-0.13
December 14, 2006	120	7	4.8	-1.10
December 23, 2006	138	10	5.4	0.48
December 26, 2006	296	44	7.0	-0.41
January 16, 2007	191	21	5.4	0.10
January 25, 2007	226	26	6.2	-0.31
May 12, 2007	101	44	4.9	-0.41
July 23, 2007	155	31	6.0	-0.41
August 9, 2007	201	4	5.9	-1.41
September 6, 2007	155	54	6.6	0.60
October 11, 2007	92	80	5.2	0.27
October 17, 2007	176	42	5.7	0.01
November 28, 2007	91	69	5.4	-0.94

767

768 **Table 9:** Amplitudes and phases of the annual gravity change at HS from different
769 sources

Source	Amplitude (μgal)	Phase (º)
Observation (T48)	6.24	-26.07
Ground water	5.48	-88.95
Atmosphere	2.98	-135.34
Soil moisture	1.41	-14.04
Polar motion	1.58	-13.98

770

771 **Table 10**: Modeled and FG5-observed rates of gravity change (in μgal year^{-1}) at HS

Source	Rate
Atmosphere	-1.3
Ground water	3.8
Soil moisture	0.5
Polar motion	0.4
Free-air motion of site	-0.1
Total	3.3
FG5 observations	2.2

772

Figure captions

Figure 1. Geological settings around the Hsinchu SG station and distributions of GPS and tide gauge stations. The meanings of the formations are explained by documents in the Central Geological Survey of Taiwan (http://www.moeacgs.gov.tw).

Figure 2. A cross-section along the alluvium north of HS showing layers with shallow and deep groundwater. Deep groundwater takes time to fill and will delay groundwater-induced gravity change. The sampling points A, B, C, D and E are shown in Figure 1.

Figure 3. Variations of coordinates at the HCHM, TCMS, SHJU and NCTU continuous GPS stations**.** The numbers in the figure panels are linear rates of displacements from least-squares fits to the coordinate variations.

Figure 4. Raw observations of SG and FG5 (top), histograms of residual FG5 gravity values after the linear regression (center), scaled SG (by the calibration factor) and FG5 observations.

Figure 5. Comparison of SG and FG5 measurements to determine the drift of T48. The FG5 gravimeter No. 228 is from France, while No. 224 and 231 are from Taiwan.

Figure 6. Tidal spectrum (in logarithm scale) from two years of raw gravity records of T48. Two clusters are present at the semi-diurnal and diurnal wave bands. Tides with periods shorter than the M_3 period are not shown here.

Figure 7. Amplitudes of ocean tide from tide gauge records at the Hsinchu Harbor (9 km to HS) and amplitudes of OTGE from the SG gravity measurements at HS (amplitudes of OTGE are the same as the ones given in the column "T48" in Table 4).

Figure 8. Gravity-atmosphere admittances at HS as a function of horizontal scale (in degree and in logarithm scale) in the cases of IB and NIB oceanic response to atmospheric pressure change. The admittances of the Newtonian effect for IB (blue square) almost coincide with those for NIB (red square).

Figure 9. Co-seismic gravity change, given as a jump (step function) in the SG gravity records at HS, due to the earthquake on September 6, 2007.

Figure 10. Observed residual gravity changes (by T48, without the body tide and ocean tide gravity effects) and modeled gravity changes at HS. The time starts

807 from March 2006.

808

809 **Figure 1**

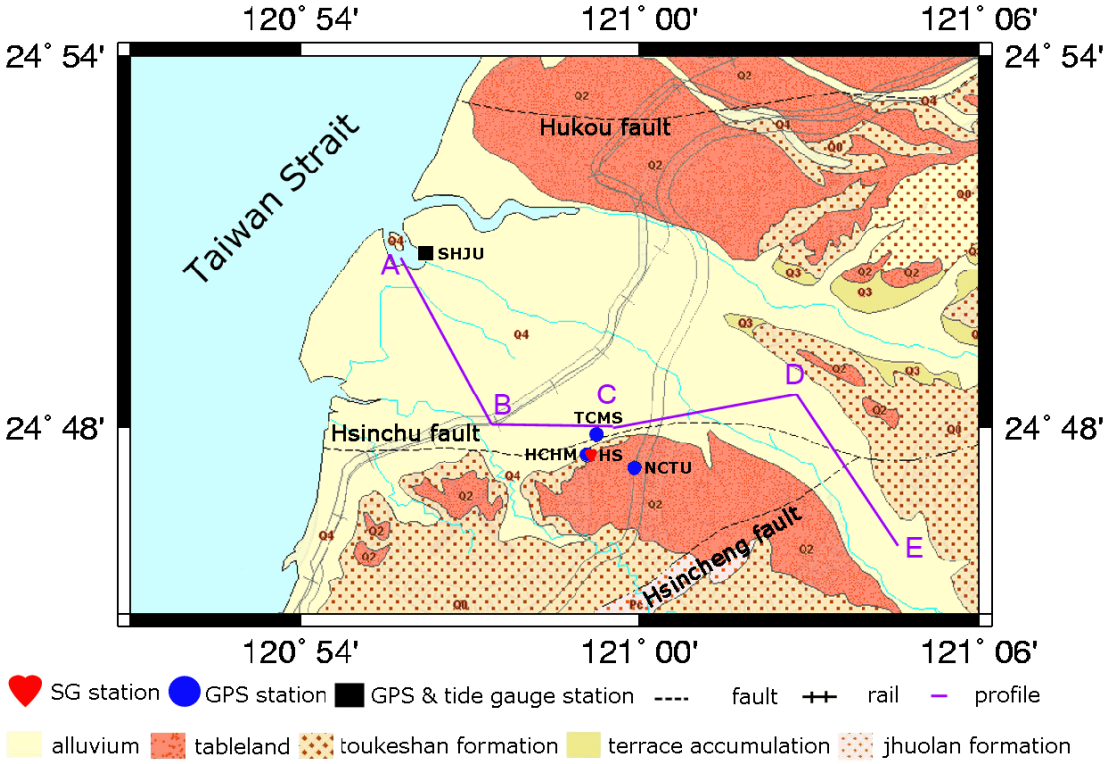

810

811 **Figure 2**

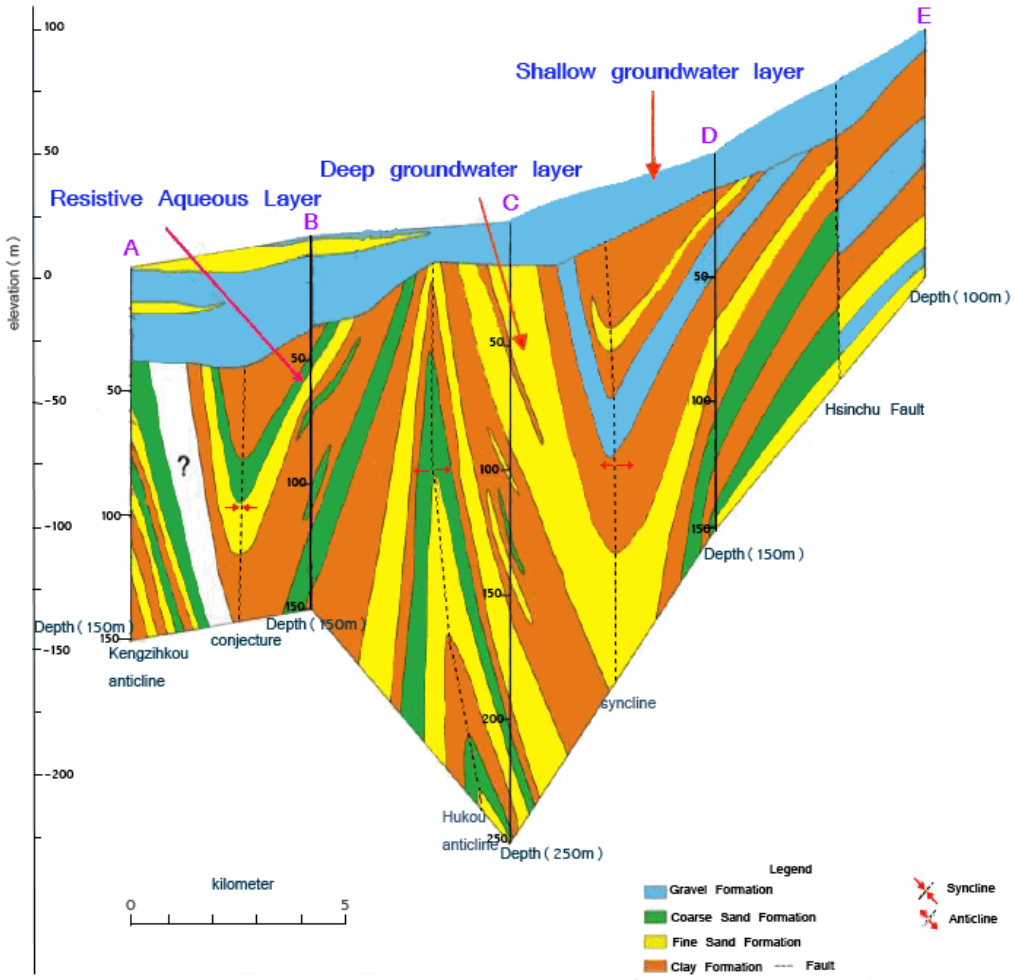

812
813

814 **Figure 3**

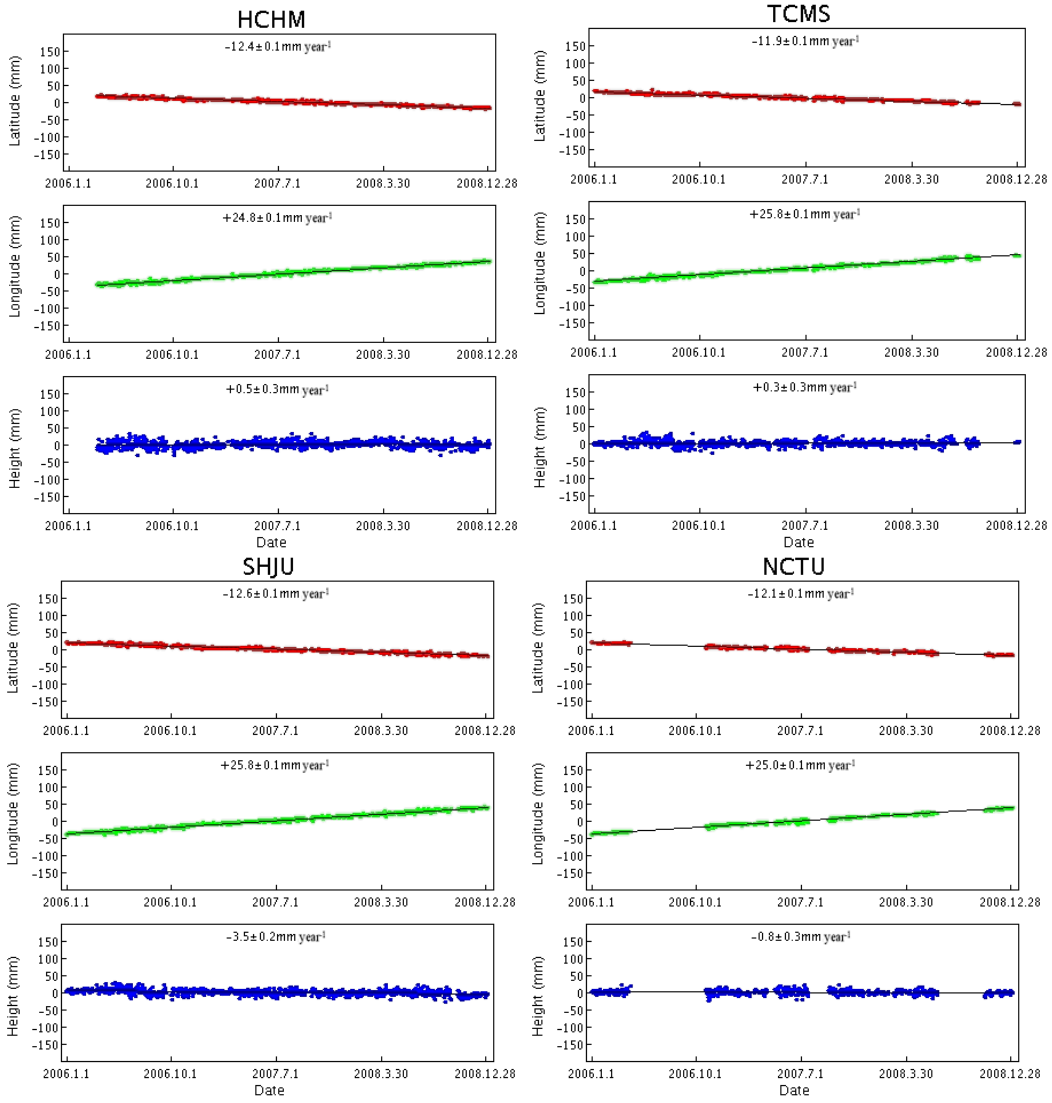

815

816

817

818

819 **Figure 4**

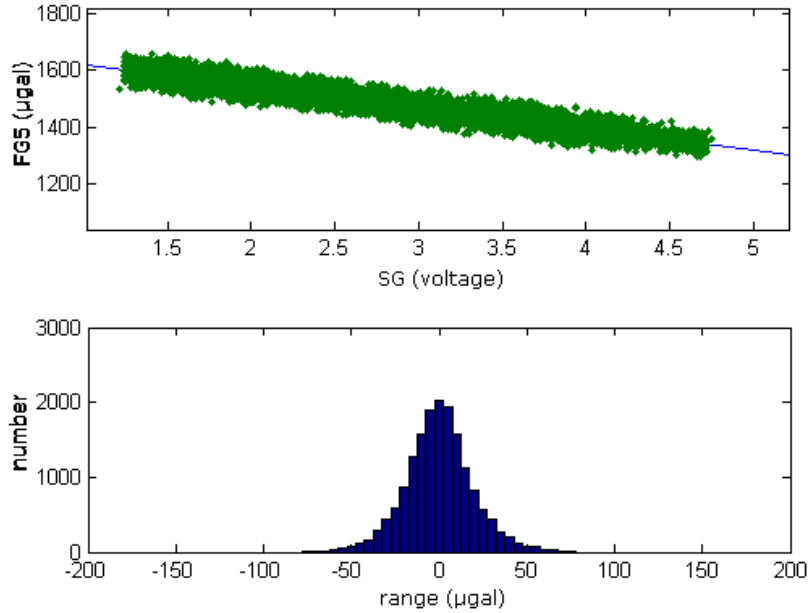

820

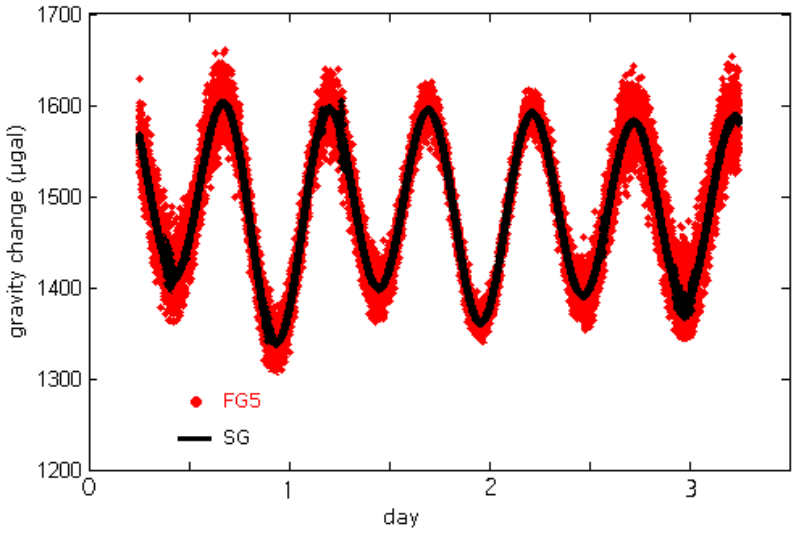

821
822

823 **Figure 5**

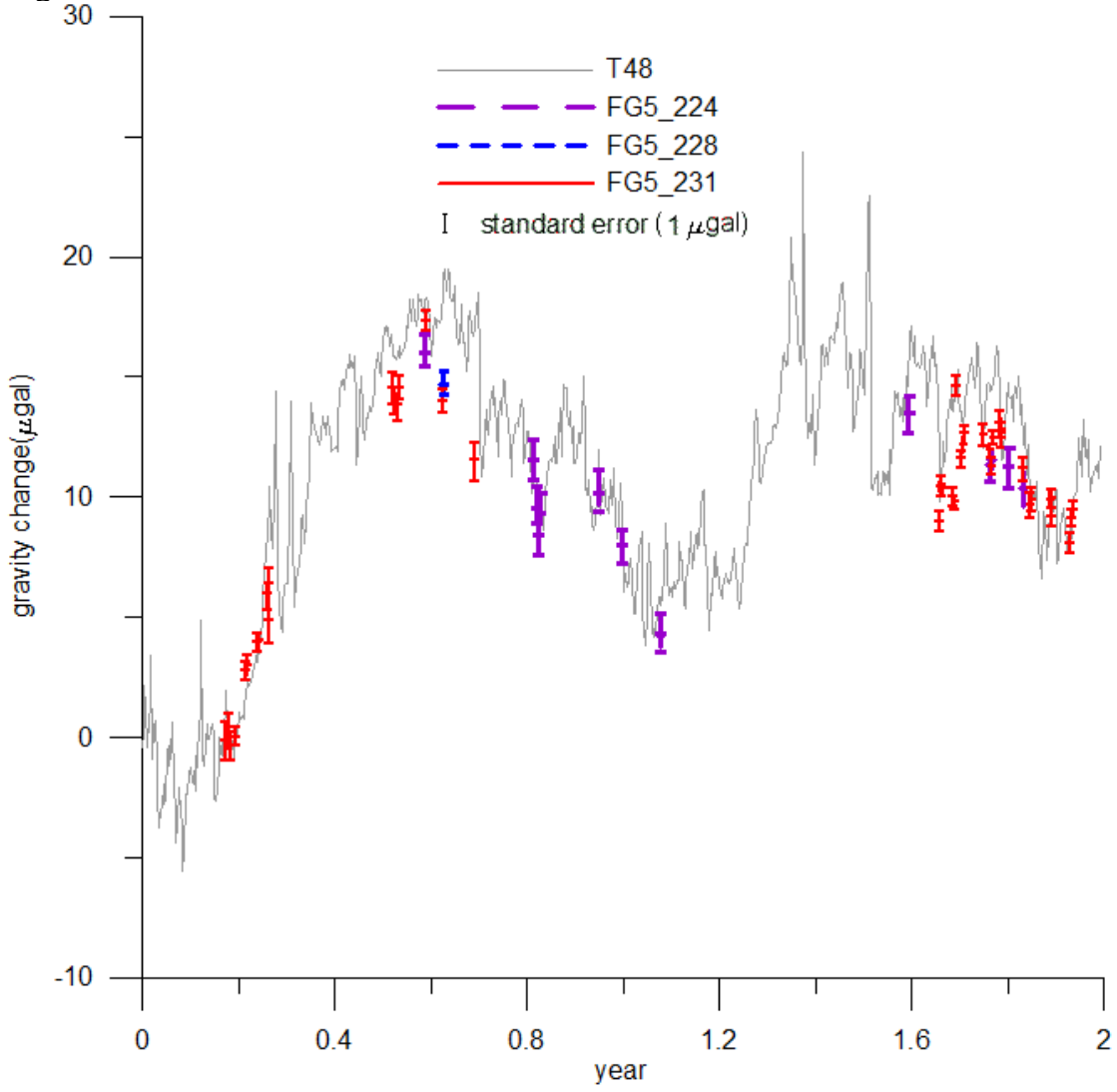

824

825 **Figure 6**

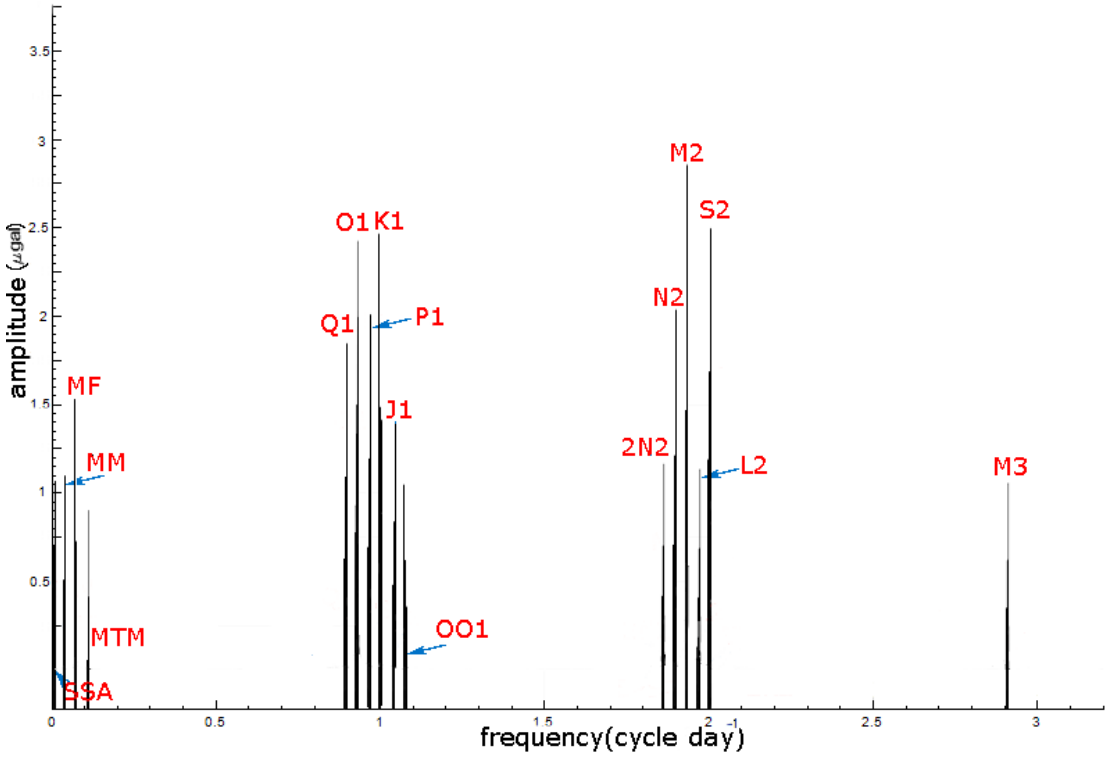

826

827 **Figure 7**

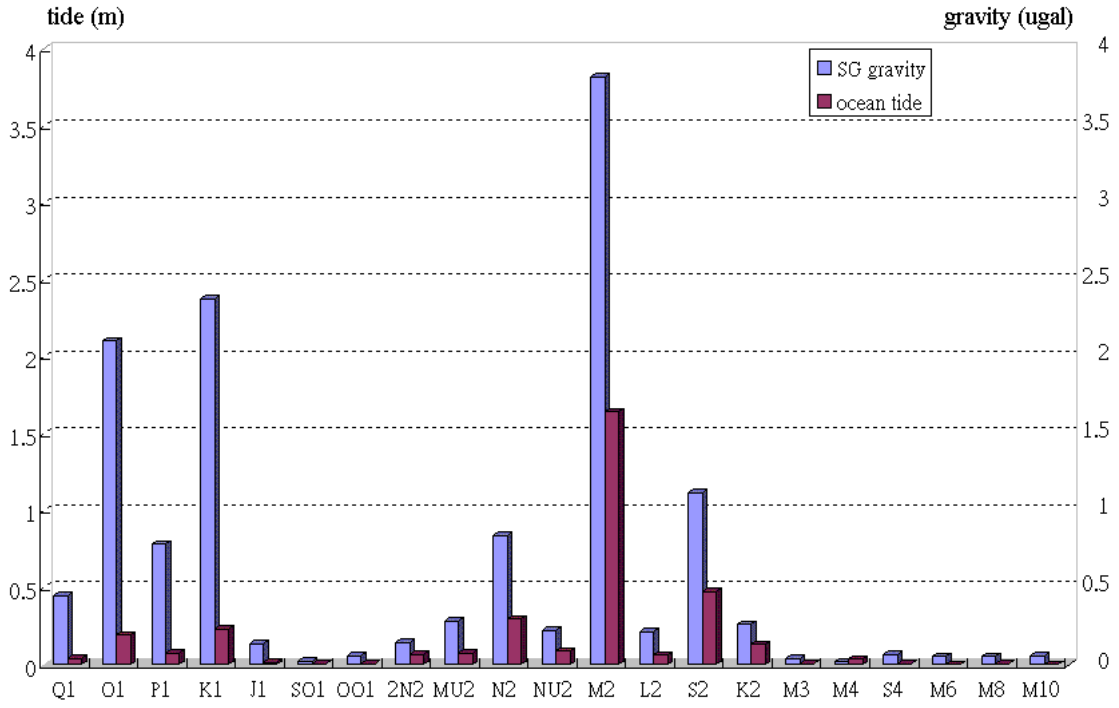

828
829

830 **Figure 8**

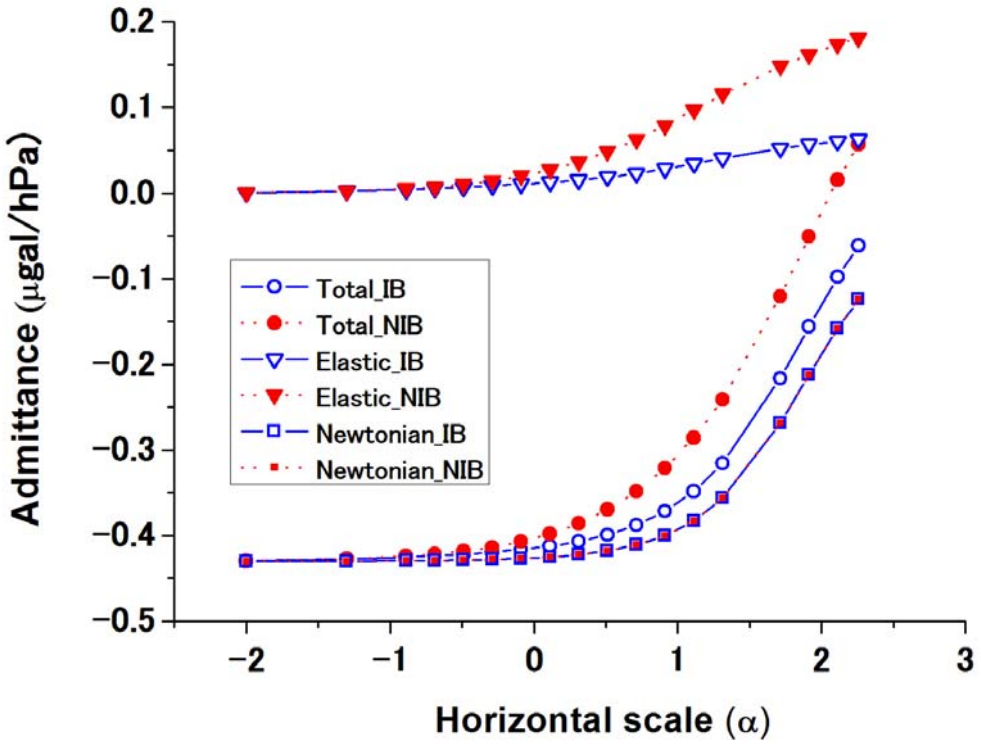

831
832

833 **Figure 9**

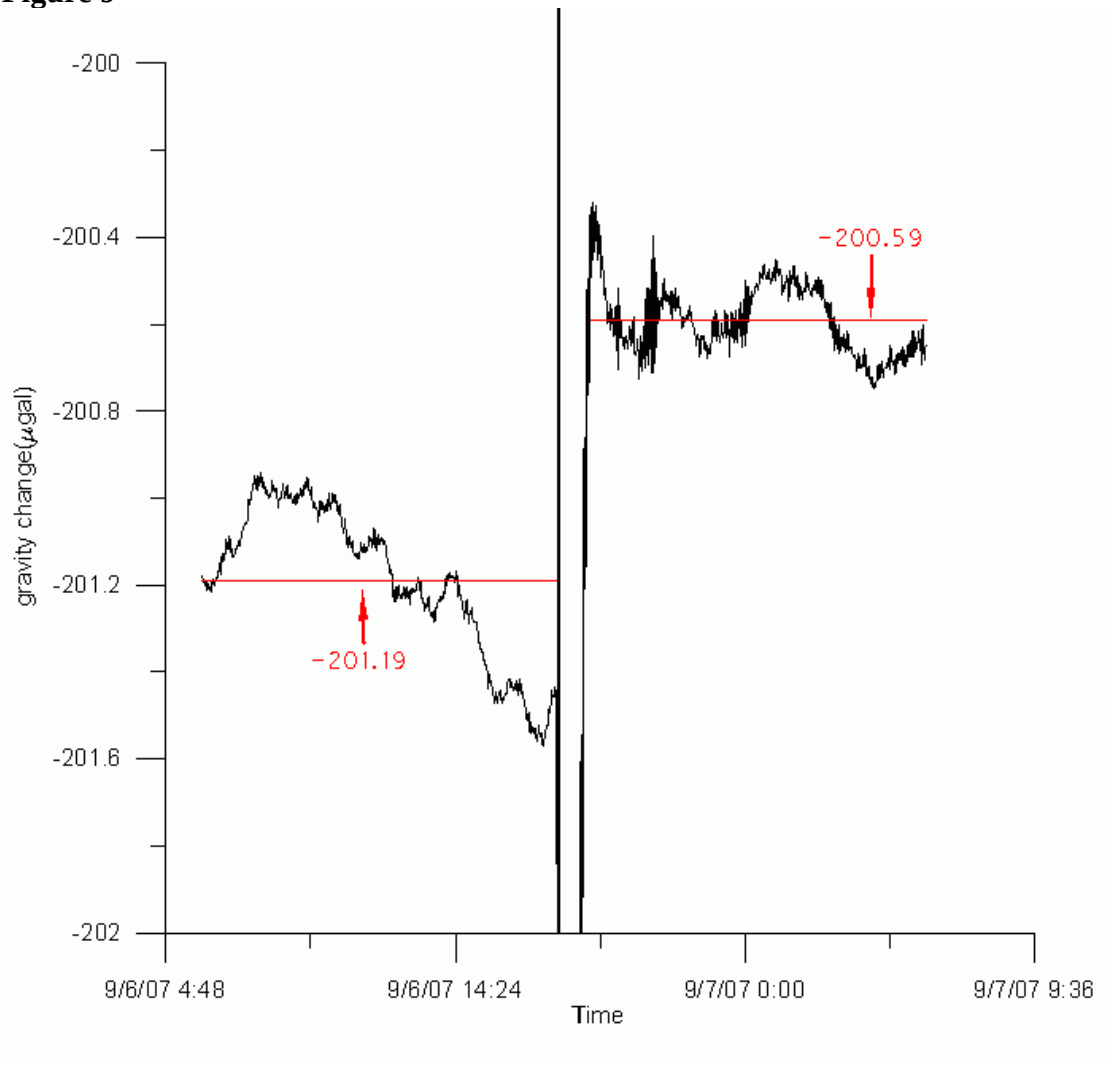

834

835 **Figure 10**
836

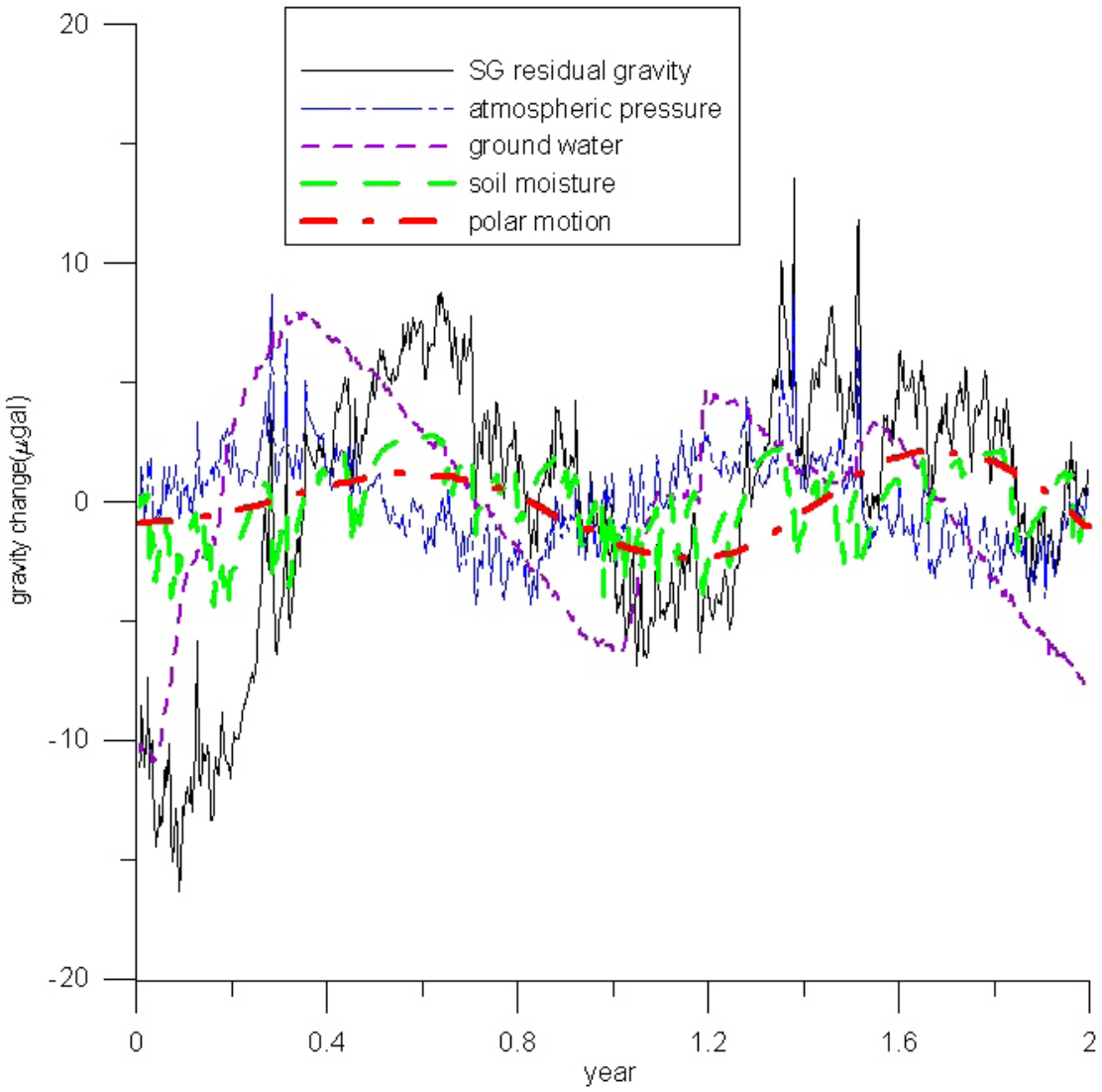

837
838